Patch-like, two dimensional WSe$_2$-based hetero-structures activated by a healing catalyst for H$_2$ photocatalytic generation

P.L. Taberna [a], J. Barros Barbosa [a], A. Balocchi [b], I. Gerber [b], K. Urita [c], A. Barnabe [a], X. Marie [b], J. Y. Chane-Ching [a,*]

[a] Université de Toulouse, UPS, CNRS, CIRIMAT, 118 Route de Narbonne, F-31062, Toulouse, France
[b] Université de Toulouse, INSA-CNRS-UPS, LPCNO, 135 Av. Rangueil, 31077 Toulouse, France
[c] Department of Engineering, Nagasaki University, 1-14 Bunkyo-machi, Nagasaki 852-8521, Japan

ARTICLE INFO

ABSTRACT

2D photoactive materials may offer interesting opportunities in photocatalytic devices since they combine strong light absorption and shortening of charge carriers' diffusion path. Because of their high surface defect concentration and the formation of a majority of edge/plane vs plane/plane contacts between the anisotropic building blocks, surface defect passivation and improvement of charge carrier transport are critical for the large development of high surface area, 2D photo-catalysts. Here, we propose a hetero-structure nanoporous network with a patch-like coating as high performance 2D photo-catalysts. The hetero-structured building blocks are composed of a photo-active WSe$_2$ nanoflake in direct contact with both a conducting rGO nanosheet and an ultrathin layer of healing catalyst. The resulting nanoporous film achieves a H$_2$ evolution photocurrent density up to 5 mA cm^{-2} demonstrating that the patch-like hetero-structures represent an effective strategy to simultaneously improve hole collection, defect passivation and charge transfer. These hetero-structures made of an ultrathin healing catalyst layer represent promising building blocks for the bottom-up fabrication of high surface area photocathodes particularly for 2D photo-catalysts displaying high defect concentration.

1. Introduction

Hydrogen production from photocatalytic solar water splitting represents a critical step for clean, efficient renewable and sustainable energy conversion [1,2]. Intense researches on various synthetic processes including Physical Vapor Deposition [3], Chemical Vapor Deposition [4], soft chemistry [5], or self-assembly of nano-sized building blocks [6] were devoted to the design and fabrication of efficient nano-structured photo-electrodes in order to greatly increase their performances. The best photo electrode nanostructures [4–5] for solar water splitting generally exhibit high surface area, defect-free, highly crystallized photoactive materials which are usually achieved at high temperatures, T > 450 °C. Designing innovative and more efficient photo-catalyst nanostructures remains a prerequisite for the large scale development of solar photocatalytic water splitting. Various strategies have been proposed for film nano-structure optimization including formation of intimate nanojunctions between a photoactive material and a catalyst [7], nanopore size control [5], or achievement of a low proportion of high-angle grain boundaries between primary crystallites forming the photoactive film [4]. Recently, new opportunities have emerged with the discovery of the vast library of 2D materials displaying unique optoelectronic properties [8-10]. Indeed, the high anisotropic form factor displayed by these 2D materials favors maximum sunlight harvesting and promotes the mass transfer of reactants and products. More important, these 2D materials may drastically shorten diffusion length of photo-generated charge carriers thus minimizing their recombination. Interestingly, these 2D materials can develop increased contact areas between the photoactive nanosheets and planar co-catalysts which are beneficial for the separation of electrons/holes by diminishing the barrier for electron transport through the co-catalyst. Thus, particular attention has been paid to the formation and role of 2D/2D interfaces. Recent construction strategies for the photocatalytic decomposition of pollutants or for the hydrogen evolution reaction proposed 2D/2D heterojunctions [11–15] including p/n hetero-junctions [11] or co-catalyst/photoactive nanosheets hetero-structures [11]. Among these 2D materials, 2D Transition Metal Di

* Corresponding author.
 E-mail address: chane.jy@gmail.com (J.Y. Chane-Ching).

Chalcogenides (TMDC) nanosheets and nanoflakes are interesting photo-active materials [9] combining unique light absorption properties [16] with appropriate band conduction levels for the Hydrogen Evolution Reaction (HER) [17–18]. In particular, TMDC materials are ideal candidates for tandem cells fabrication because they display different HER onset potentials and adjustable band gaps depending on their chemical composition [19–20] and thickness, i.e. varying from monolayer to a few layers [9]. Despite the recent development of 2D photocatalysts, they still face several significant challenges: (1) The high concentration of surface defects of these 2D materials [21] acting as recombination sites for the charge carriers, has greatly hampered the development of these materials in photo-catalysis. Various strategies have been already proposed to passivate these defects [6,22–23], improving their performances in water splitting. Particularly, the design of a multicomponent film achieving defects passivation and possessing catalytic properties [6,24] should offer the advantage of a better control of the film microstructure. (2) Another important obstacle hindering their development in practical applications is their low surface area [8]. Although recent efforts have focused on the design of macroporous architectures [25], their nanoporous counterparts constructed from these 2D materials yielding higher surface areas generally suffer from poor charge carrier transport due to a majority of edge/edge or edge/plane vs plane/plane contacts. Thus, it is highly desirable to develop innovative routes for the design of new nanostructured films fabricated from 2D photo-catalysts and displaying high photo-electrochemical performances.

In this work, a nanoporous network of patch-like hetero-structures fabricated from 2D WSe_2 nanoflakes and including an ultrathin layer of healing co-catalyst is proposed for the photocatalytic water splitting. 2D WSe_2 was chosen as an ideal 2D candidate because of its band gap (1.5 eV) closely matching the solar spectrum [9] and its high stability in acidic or alkaline solutions. The hetero-structured nanoporous network have been first designed to improve the photo-generated hole collection through the implementation of a percolating network of conducting reduced Graphene Oxide (rGO) nanosheets connected to the Fluorine-doped Tin Oxide (FTO) back electrode. Taking advantage of their analogous layered structures, we have thus focused in a first step on the construction of WSe_2/rGO layered heterojunctions with partial coverage of the WSe_2 surface by the rGO nanosheets. The patch-like, high surface area, layered hetero-structure was prepared in this first step by a colloidal co-self-assembly process of WSe_2 nanoflakes and Graphene Oxide (GO) nanosheets of lower lateral size in dimethylformamide (DMF). GO nanosheets which were later transformed into rGO by thermal reduction under Ar atmosphere, were chosen because they interact with the WSe_2 nanoflakes by amphiphilic interactions [26]. Indeed, GO nanosheet acts as an amphiphilic surfactant, in binding to WSe_2 through the hydrophobic, un-oxidized, poly-aromatic islands located in its basal plane while the hydrophilic (i.e. carboxyl and hydroxyl) groups on the edges ensure the colloidal stabilisation of the GO/WSe_2 ensemble in DMF. In addition to this amphiphilic interaction, the formation of the WSe_2 nanoporous layered hetero-structure was driven by short-range complexing interactions between the WSe_2 surface and a sacrificial template. For this purpose, a customized nanometer-size, colloidal, mixed-metallic sulfide ($Sn_{0.5}Sb_{0.5}S_{1.5}$) template interacting with the TMDC nanoflakes surface was specially-engineered and synthesized to ensure minimal oxidation of the WSe_2 thin nanoflakes during the whole self-assembly process. In a second step, simultaneous surface defect passivation of the photoactive 2D WSe_2 and its catalytic activation were performed yielding a co-catalyst/ WSe_2/rGO hetero-structure network. To preserve its high surface area, we have homogenously coated the photoactive film using a multicomponent ultrathin film displaying multifunctional properties. This film composed of different thio- and oxo-thio-Mo complexes denoted in the following Mo_xS_y, includes thio- and oxo-thio-Mo monomers with healing properties while the presence of thio- and oxo-thio-Mo dimers and trimers provides catalytic properties [6]. Using high resolution transmission microscopy (HR-TEM) and

intensity modulated photocurrent spectroscopy (IMPS), we demonstrate that the patch-like coating of the WSe_2 photo-active surface is composed respectively of the rGO conductive nanosheets and the healing co-catalyst film. High photocurrents up to 5 mA cm^{-2} under 1 sun illumination were achieved highlighting the beneficial use of a healing co-catalyst in the fabrication of these patch-like hetero-structures.

2. Methods

2.1. Materials

2.1.1. Preparation of Sn(IV)-Sb$_2$S$_3$ (Sb   0.5 M) colloids
$SbCl_3$ (Sigma, 8 mmol, 1.83 g) and $SnCl_4$ 5H$_2$O (Sigma, 8 mmol, 2.8 g) are dissolved in 32 ml dimethylsulfoxide (DMSO). A $(NH_4)_2S$ aqueous solution is prepared by adding H$_2$O to 3.23 M S^{2-} solution (Sigma, 64 mmol, 19.81 ml) to a total volume of 128 ml. Precipitation of a brown solid is observed after the instantaneous addition of the DMSO metallic salts solution to the sulfide solution. After stirring one night at room temperature (RT), the reaction mixture is aged at 30 °C (two days) until a yellow limpid solution containing the anionic metallic chalcogenide species is obtained. After dilution of the freshly prepared anionic chalcogenide solution (20 ml of the mother solution diluted to 200 ml by H$_2$O), temperature polycondensation of the soluble anionic species is performed in a pre-heated constant temperature bath at 65 °C. When the solution turns to yellow green turbid (2 h), the reaction is immediately quenched by addition of 200 ml H$_2$O to the solution. After aging for one night at RT, the colloidal solution is washed on a 3 KD membrane by 200 ml H$_2$O and finally post-concentrated by ultrafiltration yielding an orange colloidal dispersion. Transfer into DMF is performed by adding DMF into the aqueous dispersions and slow evaporation for 16 h in Air atmosphere at 65 °C.

2.1.2. WSe$_2$/rGO co-textured powder formation
WSe_2 powder (Alfa Aesar) was exfoliated in solvent [27] using a 750 W ultrasonicator at 40% amplitude. The Di Chloro Benzene (DCB) solvent-exfoliated WSe_2 nanoflakes were collected after size-fractionation (selection at 800 rpm) and redispersion in DMF. The WSe_2 (40 g l^{-1}) and $Sn_{0.5}Sb_{0.5}S_{1.5}$ (100 g l^{-1}) DMF concentrated colloidal dispersions were mixed at room temperature at a WSe_2 volume fraction, Φv_{WSe2}, Φv_{WSe2} $V_{WSe2}/(V_{WSe2} + V_{SnSbS})$ 0.15. Then, 1 ml of GO dispersion (1 g l^{-1}, lateral size L   80 nm) was added to the previous mixture to achieve r$_{rGO}$ rGO/(rGO + WSe_2)   0.05 M ratio. The resulting solution was poured into a large surface open reactor and evaporated at room temperature under a hood equipped with Air flow. The resulting dried co-textured powder was collected and calcined under Ar at 200 °C for 1 h. Dissolution of the template from the co-textured powder was performed by adding 20 ml of $(NH_4)_2S$ 1.5 M. This operation was performed 3 times and the powder was finally washed in H$_2$O. No trace of Sn or Sb was detected by energy dispersive spectroscopy (EDS) analysis on the WSe_2/rGO dried co-textured powder.

2.1.3. WSe$_2$/rGO photo-electrodes
The photo-electrodes were made by drop casting a solution containing the WSe_2/rGO co-textured powder previously described (r$_{rGO}$ 0.05) dispersed in a GO colloidal aqueous solution to achieve a total rGO content, r$_{rGO}$ 0.15. Two sets (4 and 8 layer stacks) of WSe_2/rGO photoelectrodes (S   1 cm^2), denoted hereafter nanostructured films, were prepared with solvent (H$_2$O) evaporation between each layer deposition. Typical average thicknesses of the films were e   2 and 4 μm respectively, obtained with mass loading, m   2 and 4 mg. The WSe_2/rGO electrodes were post-calcined with a heating rate of 25° h^{-1} under Ar at 350 °C for 2 h.

2.1.4. MoxSy healing co-catalyst film deposition
A thio-, oxo-thio-Mo complexe solution is prepared as previously described [6] by dissolving 2.5 mmol of $(NH_4)_2$ MoS_4 (0.65 g), into 8 ml

of 0.31 M $(NH_4)_2S$ solution. The solution is adjusted to pH 9 with 4.5 ml of HCl 0.5 M and diluted to 250 ml. Solid precipitate in small quantity is removed by ultracentrifugation at 15 000 rpm for 10 min. The healing catalyst film is deposited by successive dip coatings (2x 16 h) of the WSe_2/rGO–FTO photo-electrode under slow stirring into the thio-, oxo-thio-Mo complexes solution (0.01 M Mo) previously prepared.

2.2. General characterization

Conductivity measurements were performed using a Signatone S 1060R conductimeter equipped with four QUAD PRO electrodes. Measurements were performed on drop-cast and nanostructured WSe_2-based films deposited on Glass substrates with ~2 μm film thickness and 1.6 mm electrodes inter-distance.

Continuous wave photoluminescence (PL) has been performed on the non-coated and co-catalyst coated WSe_2 photocathodes by exciting the samples mounted on an AttoCube atto 700 cryostat with a He-Ne laser (excitation 632.8 nm). The laser light has been focused on the sample using a high numerical aperture lens (NA 0.55) to a ~2 μm spot-size with powers ranging from 50 to 500 μW. The PL signal, collected from the sample in backscattering geometry, has been dispersed by an imaging spectrometer and the spectrum recorded using a liquid nitrogen-cooled silicon charge coupled device (CCD camera).

TEM studies were performed using a JEOL JEM-ARM 200F spherical-aberration probe corrected electron microscope equipped with a cold field emission gun operated at 200 kV. The complete equipment includes an ultrafast Ultrascan 2 k × 2 k camera (Gatan) for TEM, high-angle annular dark field (HAADF) detectors (JEOL) for STEM imaging, a Centurio X-ray detector (JEOL) for ultra-high resolution EDS mappings. Plan view sections were prepared by Focussed Ion Beam (FIB), the sample has been thinned by standard tripod polishing to a thickness of a few μm. The final sample is thinned using a Gatan PIPS 691 ion beam miller to create an electron transparent sample.

2.3. Hydrogen and photo-electrochemical measurements

Linear scanning voltammetry (LSV) curves were recorded using a Gamry potentiostat in a three-electrode configuration equipped with a Pt foil and a Ag/AgCl reference electrode. In a typical LSV acquisition, the voltage applied to the working electrode (S 1 cm^2) was swept cathodically (10 mV s^{-1}) between +0.4 V and 0.4 V vs NHE in H_2SO_4 0.5 M for the Mo_xS_y/WSe_2/rGO electrode. The light source used in the photoelectrochemical (PEC) measurements was a 100 W Xe lamp including an AM 1.5G filter. By adjusting the distance between the sample and the simulator, we finely controlled the irradiance of 1 sun measured by a Solar light PMA 2144 pyranometer.

A three electrode closed set-up was used for the hydrogen detection. The real-time analysis of the composition of the gas was performed using a Gas Chromatograph (Shimadzu, GC-2014 AT). The Faradic efficiency of our cell is calculated assuming 100% efficiency for a Pt calibration cell equipped with Pt foils as both the working electrode and the counter electrode.

Incident-photon-to-current-efficiency (IPCE) measurements of the photocathodes were performed illuminating the photocathode using a set of high-power light emitting diodes (H2A1 Series LED) from Roithner Laser Technik.

IMPS measurements were performed in H_2SO_4 0.5 M for the bias range +0.4 to 0.2 V vs NHE and a frequency range 0.1 Hz to 10 KHz. The modulated illumination was provided by a light emitting diode (Roithner Laser Technik, λ 760 nm, 0.4 Watt). The AC amplitude was set up to 40% of the applied DC base intensity.

3. Results-Discussion

3.1. 2D WSe_2 nanostructured film by co-self-assembly

Fabrication of the 2D WSe_2 nanostructured photocatalyst involves the colloidal co-self-assembly of GO nanosheets, WSe_2 nanoflakes of optimal thickness and a post leachable template of controlled size (D 65 nm, Fig. 1a). In a first step, we prepare nanoporous co-textured WSe_2/rGO powder by colloidal self-assembly in DMF of GO nanosheets, solvent-exfoliated WSe_2 nanoflakes and spherical $(Sn_{0.5}Sb_{0.5}S_{1.5})$ colloidal templates (Fig. 1b,c and Fig. S1). Indeed, Sb_2S_3, which forms highly soluble complexes with sulfide anions [28], proves to be a good candidate as a hard template. Sn(IV) cations were incorporated into Sb_2S_3 to significantly improve the colloidal stabilization of the Sb_2S_3 nanoparticles while providing molecular Sn chalcogenides as surface ligands [29,30]. To fully exploit the layered character of the photoactive film, we select ultrathin GO nanosheets of slightly lower lateral size as building blocks to construct the conducting percolating network. GO nanosheets, instead of graphene [31,32], were used to favour amphiphilic interactions with the WSe_2 nanoflakes building blocks [26] during the co self-assembly process. With the objective to conduct the co-self-assembly in a highly repulsive regime, $(Sn_{0.5}Sb_{0.5}S_{1.5})$ colloids and GO nanosheets building blocks were prepared in a highly alkaline aqueous solution (Fig. S1), thus developing similar negative surface charge. To prevent any phase separation with the WSe_2 nanoflakes, the co-self-assembly process was driven in DMF solvent. After solvent evaporation, thermal consolidation of the WSe_2/rGO network under Ar at 200 °C and post-dissolution of the $(Sn_{0.5}Sb_{0.5}S_{1.5})$ template in S_2^{2-} aqueous solution, a composite textured powder is collected. To get more insight into the interactions driving the co self-assembly process, we first separately conducted self-assembly of WSe_2 nanoflakes and of GO nanosheets with the $(Sn_{0.5}Sb_{0.5}S_{1.5})$ colloids template. BET measurements performed on the corresponding dried textured powders clearly show the presence of significant pore volume exclusively on the textured WSe_2 sample (Fig. S2). This demonstrates that the metallic sulfide colloidal template interacts preferentially with the WSe_2 nanoflakes and not with the GO surfaces. In addition, no phase separation of the GO nanosheets was observed during the co-assembly. Thus, our process probably involves a second interaction regime based on amphiphilic interactions between WSe_2 nanoflakes and GO nanosheets [26] as previously reported.

To improve percolation of the rGO network, additional infiltration of GO nanosheets was performed by drop-casting mixed solutions containing free-standing GO nanosheets in addition to the co-textured WSe_2/rGO powder prepared as previously described. After air evaporation, a calcination step was performed at 350 °C (12 h ramp time) under Ar to convert GO into rGO. It is worthy to note that the long duration time of the calcination step improves connection between the WSe_2/rGO co-textured powder thus yielding a nanoporous film composed of layered WSe_2/rGO building blocks. These nanostructured films, denoted hereafter nanostr. WSe_2/rGO films, exhibit r_{rGO} 0.15. For comparison, two reference films were prepared using i) rGO-free textured WSe_2 powder, denoted nanostr. WSe_2/rGO-free films and ii) exfoliated WSe_2 nanoflakes prepared in similar exfoliation and selection conditions –but without self-assembling- which were simply drop-cast, denoted drop-cast WSe_2 films.

Because WSe_2 nanosheets are sensitive to oxidation, chemical degradation of the nanostructured WSe_2/rGO films prepared from WSe_2 nanoflakes exfoliated in air atmosphere was assessed by X-ray photoelectron spectroscopy (XPS) (Fig. S3). From the data extracted from the W 4f (WSe_2, B.E.: 31.7; 33.7 eV) and Se 3p regions, we determine Se/W_{molar} 2, indicating the absence of significant WSe_2 degradation. A more quantitative value of the oxidation ratio, $r_{W..O}$ W..O / (W..O + W..Se), $r_{W..O}$ 0.135, was extracted from 4f 7/2, 4f 5/2, tungsten oxide (WOx) peaks (B.E. 35.3 and 37.4 eV, [33,34]) confirming a low oxidation ratio. Because a similar value of $r_{W..O}$ was observed on freshly
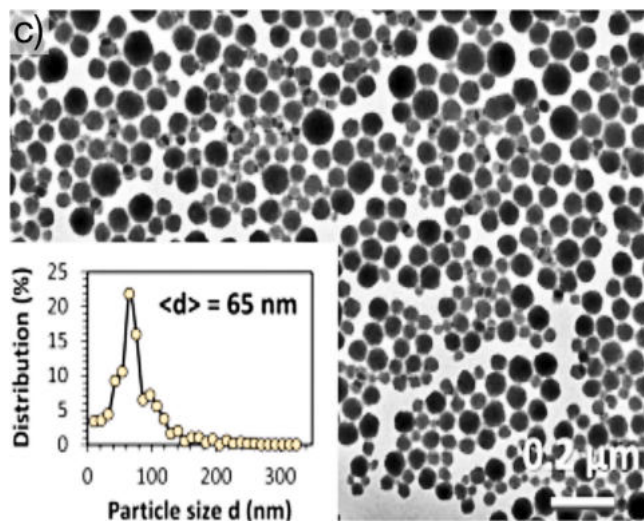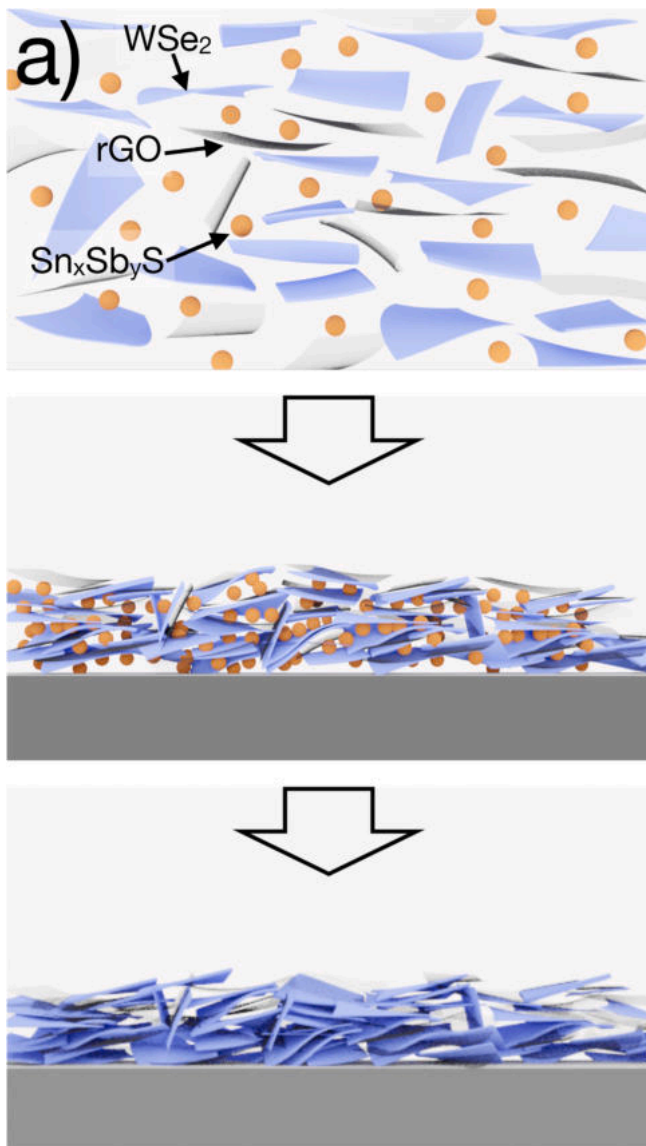
Fig. 1. a) Schematic of the co-self-assembly process. b) Photograph of (Sn$_{0.5}$Sb$_{0.5}$S$_{1.5}$) template colloidal dispersion in DMF c) TEM image showing monodisperse spherical (Sn$_{0.5}$Sb$_{0.5}$S$_{1.5}$) colloids.

exfoliated WSe$_2$ nanoflakes, the slight oxygen contamination observed thus mainly arises from the exfoliation process performed in air atmosphere. This result also demonstrates that no significant chemical oxidation of the WSe$_2$ nanoflakes occurs during the whole co-self-assembly process including the GO thermal reduction step when using WSe$_2$ building blocks selected at 800 rpm. Importantly, the cyclic voltammetry curves recorded on the nanostr. WSe$_2$/rGO-free film prepared from WSe$_2$ nanoflakes selected at 800 rpm show an enhancement of the electrochemical surface area. A 4-fold increase of the capacitance compared to the drop-cast photo-electrode is observed revealing a remarkable improvement of the electrochemically accessible surface area with nanostructuration (Fig. 2).

A typical cross-section SEM image of the nanostr. WSe$_2$/rGO film recorded at relatively low magnification after sequential slicing using FIB milling is shown in Fig. 2a. We can clearly observe a porous skeleton composed of interconnected building blocks displaying anisotropic morphology. The presence of W and Se shown by EDS analysis in these anisotropic building blocks demonstrate that these building blocks can be fully identified as WSe$_2$ nanoflakes. Fine inspection of this SEM image reveals that the photoactive film contains bundles of WSe$_2$ nanoflakes of average lateral dimension, L   400 nm, and thickness, e   100–120 nm, each bundle being composed of an in-plane stacking of ~ 3 primary nanoflakes of ~ 40 nm thickness (Fig. 2b). Consistently with this thickness value determined from a small probed volume, a similar thickness value was calculated from the experimentally determined BET surface area of 7 m^2 g^{-1} (Details in Fig. S2). Moreover, from an in-depth X-ray investigation and using a Williamson-Hall model [35], two sets of data are clearly observed yielding two different plots resulting from the anisotropic morphology of the ordered domains (Fig. S4). As expected, larger ordered domain size is observed for the diffraction peak of the (00l) basal plane. More important, the ordered domain size determined for the (100), (105) diffraction peak (e   46 nm) is in line with the primary building blocks thickness of the WSe$_2$ nano-flakes determined from SEM picture (Fig. 2a, 3a). These values determined on a nano-structured film free from preferential orientation indicate that these

primary nanoflakes are indeed monocristalline. The intimate mixture of rGO nanosheets and WSe$_2$ nanoflakes is illustrated on Fig. 2c showing a rGO nanosheet coating the WSe$_2$ nanoflake. Although the partial extension of the rGO nanosheet beyond the WSe$_2$ nanoflake was clearly observed, thus favoring the formation of a percolated network of rGO nanosheet till the back FTO electrode, several clues confirm that the WSe$_2$ nanoflakes are intimately coated by the rGO nanosheets. First, nanostructured WSe$_2$ powders prepared with and without rGO were shown to display nearly similar pore volume, pore distribution and BET surface area (Fig. S2a,b). In addition, although slightly lower, a similar order of magnitude for the electrochemically active surface was determined by voltammetry (j-V curves, Fig. 2e) in 0.5 M H$_2$SO$_4$ both for the nanostructured WSe$_2$/rGO photo-electrodes prepared from the co-textured WSe$_2$/rGO powder and for a reference nanostructured rGO-free WSe$_2$ powder. Taking in account that the rGO ratio incorporated into the film is lower than the amount required for the full coverage of the WSe$_2$ nanoflakes surface (Fig. S2), all these results indicate a patch-like coating of the WSe$_2$ surface by the rGO nanosheets rather than the presence of a high proportion of free-standing rGO.

3.2. Decrease of charge carrier accumulation by construction of a percolated rGO nanosheets network

In contrast to drop-cast reference films displaying a large number of plane-to-plane contacts, the majority of contacts observed in the cross section image of the nanostructured films composed of 2D nanoflakes are edge-to-plane or edge-to-edge contacts (Fig. 2a). More specifically, the large decrease of plane-to-plane contacts should greatly affect the electrical conductivity of the film. As expected, significant decrease of the lateral conductivity over a large distance (1.6 mm) was observed on nanostructured WSe$_2$ films for measurements performed in Air atmosphere using a four-electrode set-up on WSe$_2$-Glass films (Fig. 2f). The better conductivity of the reference drop-cast film indicates reasonable long-range conductivity in the range 10^{-2} S m^{-1} resulting both from the in-plane conductivity of the primary WSe$_2$ nanoflakes [36] and from the
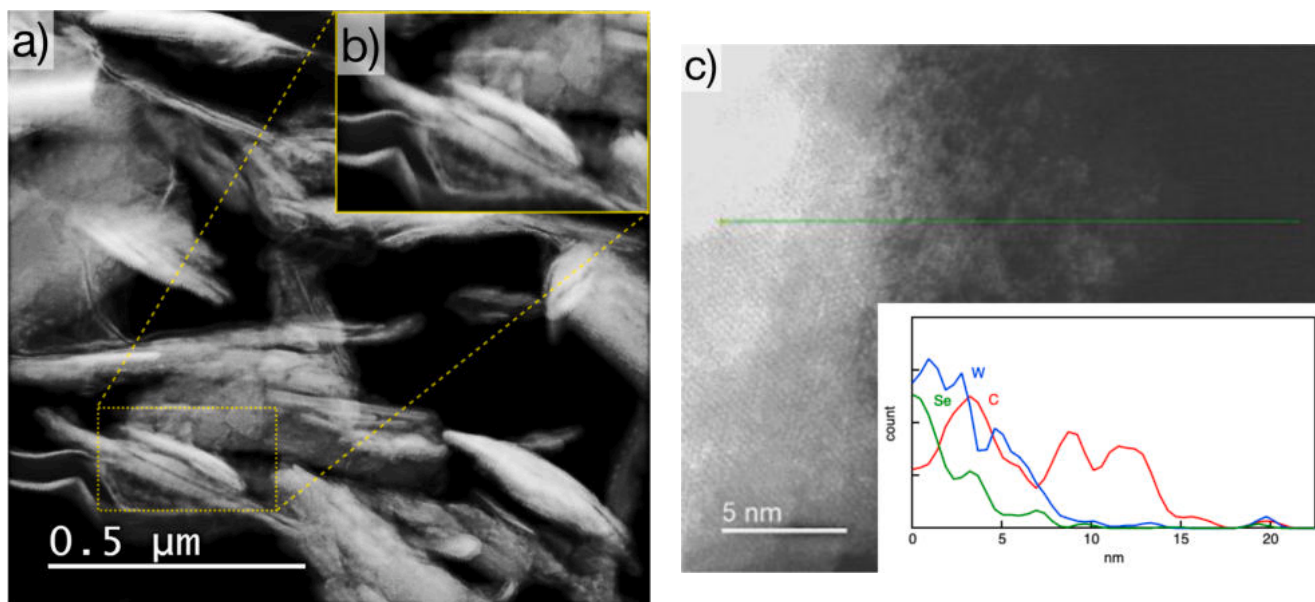

Fig. 2. WSe$_2$/rGO nanostructured 2D photocatalyst properties. a) FIB-TEM cross section image showing a percolating network of WSe$_2$/rGO nanoflakes displaying mainly edge-edge or edge-plane contacts. b) Insert: Zoom showing that the 120 nm thick, WSe$_2$ bundle is composed of 3 primary nanoflakes of ~ 40 nm. c) TEM image showing a rGO nanosheet covering a WSe$_2$ nanoflake. W, Se and C EELS spectra showing a rGO nanosheet stretching out outside the WSe$_2$ surface over 5 nm. d) Carbon, tungsten and selenium mapping showing coating of WSe$_2$ by rGO. e) Cyclic voltammetry curves recorded at 20 mV/sec in 0.5 M H$_2$SO$_4$ for the rGO-free/ WSe$_2$ and rGO/WSe$_2$ nanostructured films. Comparison with the j-V curve recorded on drop-cast WSe$_2$ reference film, given for reference highlights the high electrochemical accessible surface area for the rGO-free/WSe$_2$ and rGO/WSe$_2$ nanostructured photo-catalysts. f) In-plane electrical conductivity of nanostructured 2D rGO/WSe$_2$ and WSe$_2$ films. Data collected from a drop-cast WSe$_2$ film is also given for reference. g) LSV curves showing r$_{rGO}$ ratio dependence of photo-current. Insert: Dark EIS plots of corresponding films showing decrease of charge transfer resistance with r$_{rGO}$ ratio. H$_2$SO$_4$ 0.5 M. E =   0.2 V vs NHE.

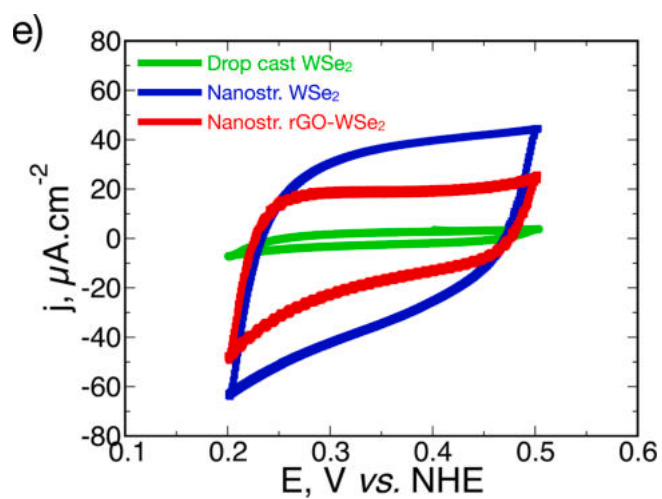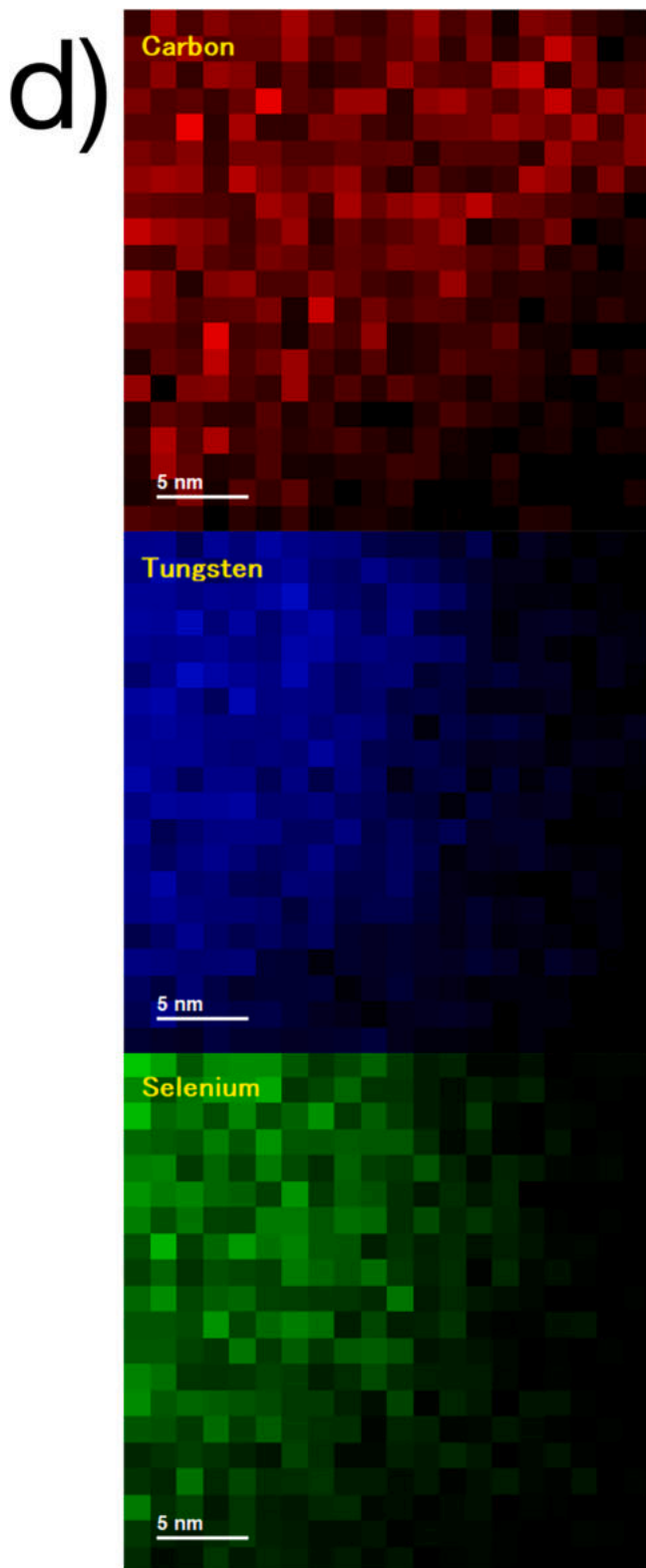d) Carbon

5 nm

Tungsten

5 nm

Selenium

5 nm

e)

Fig. 2. (*continued*).

higher number of plane-plane contacts into these films. In contrast, in the nanostructured WSe$_2$ film displaying mainly edge-to-plane or edge-to-edge contacts, the significant electrical conductivity decrease down to 10^{-4} S m^{-1} highlights the poor electrical connectivity of these contacts. Interestingly, although the rGO nanosheets produced from thermal reduction of ultra-sonicated GO were not well-crystallized, the long

range electrical conductivity was restored within the nanostr. WSe$_2$/rGO film by insertion of a low rGO concentration (0.72% wt rGO or r$_{rGO}$ 0.2).

Using a co-self-assembly process, this result demonstrates the formation of a percolated network of rGO nanosheets occurring at a rGO/WSe$_2$ surface coverage ratio σ   0.85 (for details, Fig. S2). Similarly, LSV

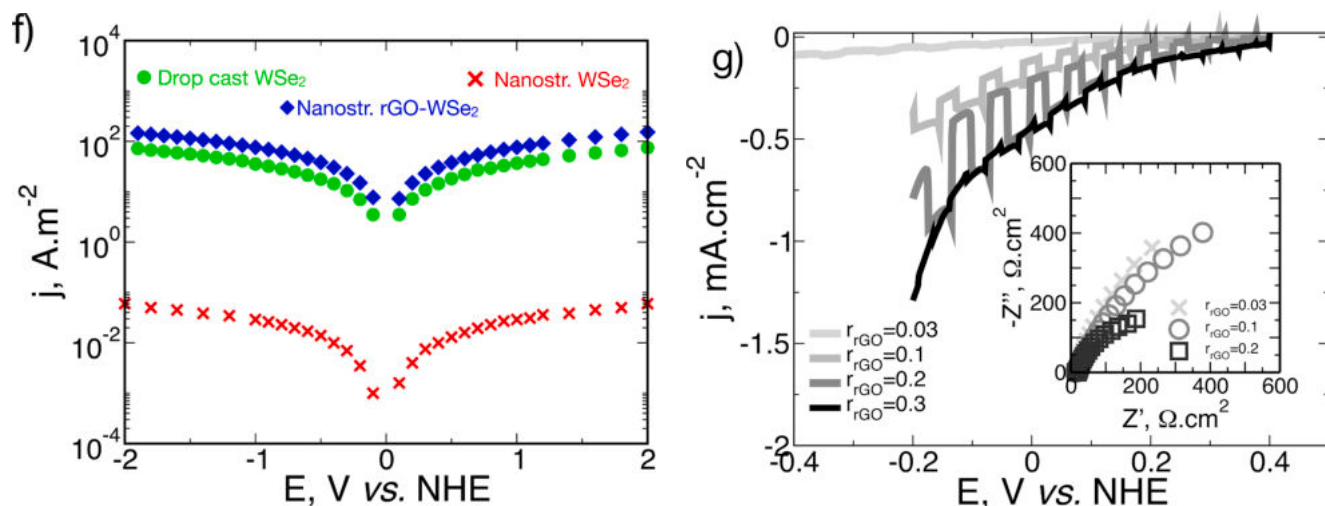curves recorded on the nanostr. WSe$_2$/rGO films show higher photo-currents for an optimal rGO ratio at r$_{rGO}$ 0.2 (Fig. 2g) in H$_2$SO$_4$ 0.5 M. More insights into the rGO contribution were gained from electro-chemical impedance spectroscopy (EIS) measurements. The lower resistance values extracted from the low frequency range of the Nyquist plots are observed at a similar optimal ratio, r$_{rGO}$ 0.20 (Fig. 2g). Because these low frequency data are associated to the semiconductor-electrolyte interface [37,38], this indicates an improved charge trans-fer at this interface occurring simultaneously with the net decrease of the charge carrier accumulation and recombination resulting from the formation of the percolating conducting network in the photoactive film (Fig. 2f,g). All these results highlight the crucial importance of improving charge carrier transport within high surface area, nanoporous photo-electrodes composed of 2D building blocks. The effects of nano-structuration implemented to the patch-like hetero-structures are demonstrated from the significant differences observed on typical LSV curves recorded on drop-cast and nanostructured WSe$_2$/rGO photo-electrodes after rGO ratio optimisation (Fig. S5).

3.3. Catalytic activation of the 2D photocatalyst by a multicomponent ultrathin film

To fully benefit from the unique properties displayed by the archi-tectured 2D WSe$_2$ photo-catalyst, an ultrathin film of healing catalyst was designed to coat intimately the partially rGO- coated WSe$_2$ nano-porous skeleton. Use of a multicomponent layer capable of both healing the WSe$_2$ surface defects and displaying a high catalytic activity [6] favours the formation of more homogeneous hetero-structures possess-ing a more uniform thickness. To preserve the short mean free-path of charge carriers relevant to these layered nanostructures, it is mandatory to efficiently passivate and catalytically activate the photo-electrode with a film thickness as thin as possible. In this context, the formation of a continuous ultrathin film was thus explored at ambient temperature in a heterogeneous growth regime from a large variety of diluted aqueous Mo sulfide complexes solutions (Mo 0.01 M, $4 \leq$ S/Mo ≤ 6, $8.0 \leq$ pH ≤ 9.7).

Best photocatalytic performances were achieved by deposition of an ultrathin film performed in low supersaturation conditions (0.01 M Mo) from a distribution of Mo sulfides complexes formed spontaneously in H$_2$O and prepared at pH 9 and S/Mo 5. In addition to the thio- and oxo-thio- Mo monomers species such as (MoS$_4$)$^{2-}$, (MoOS$_3$)$^{2-}$, an electro-spray ionization mass spectrometry (ESI-MS) investigation (Fig. S6) reveals that these solutions display peak concentrations of highly catalytically active dimers (Mo$_2$S$_{12}$)$^{2-}$ [39], (Mo$_2$S$_6$O$_2$)$^{2-}$ [40] and trimers (Mo$_3$S$_8$O)$^{2-}$. Formation of a stable, ultrathin film displaying

high photo-electrochemical performances was achieved using a selec-tive dip coating process including successive long duration time (up to 2x 16 h) alternating with H$_2$O washings [6].

Typical cross-section SEM image the co-catalyst/WSe$_2$/rGO hetero-structures was recorded after sequential slicing (Fig. 3a) using a FIB. We can clearly observe a porous skeleton composed of interconnected building blocks displaying an anisotropic morphology. Interestingly, consistently with XRD data (Fig. S4a), the presence of random orienta-tions of the WSe$_2$ nanoflake building blocks indicates a successful 3D self-assembly. Fine inspection of the interconnected network reveals the presence of irregular contours on the periphery of nanoflakes and curved domains at inter-nanoflakes junctions. This indicates the presence of a continuous film coating the WSe$_2$ nanoflakes. Although the accurate determination of the average thickness of the WSe$_2$ nanoflakes remains difficult from the SEM images, the WSe$_2$ nanoflakes exhibit an average thickness ~120 nm, close to the values previously determined on the catalyst-free WSe$_2$/rGO nanostructures. Careful observation of the SEM images also reveals the presence of higher contrast linear domains all along the co-catalyst/WSe$_2$/rGO skeleton confirming as previously observed on the nanostr. co-catalyst-free/WSe$_2$/rGO film that these anisotropic hetero-structures ~120 nm thick are indeed mainly composed of the stacking of ~3 primary nanoflakes (Insert Fig. 3a). Note that from an in-depth inspection of the sample, we cannot discard the presence of isolated WSe$_2$ nanoflakes of lower thickness. For example, better insight on the properties of the co-catalyst/WSe$_2$ interface was obtained on isolated nanoflakes of lower thickness (~8 nm thickness composed of ~12 elementary nanosheets) coated by an ultrathin film of co-catalyst (Fig. 3b). From EDS analysis, both the nanoflakes as well as the lower contrast domain coating the nanoflakes were fully identified as WSe$_2$ and co-catalyst with the respective presence of W, Se and Mo, S. Fig. 3b reveals the formation of a homogenous, compact and perfectly adherent co-catalyst coating onto the WSe$_2$ surface. Electronic diffrac-tion performed on this coating clearly demonstrates its amorphous feature. A high resolution STEM image taken at nanometer scale (Fig. 3c) reveals that the Van der Waals layered structure remains largely intact with an interlayer spacing of 0.66 nm which is within 0.5% of that reported for bulk WSe$_2$ [41]. More important, the HRTEM image also shows that the layered structure of the WSe$_2$ is preserved up to the WSe$_2$ nanoflake periphery after co-catalyst deposition without any decrease in lateral size, clearly demonstrating that no degradation oc-curs at the edges of the WSe$_2$ nanoflakes as shown in Fig. 3c. Details of the Mo$_x$S$_y$/WSe$_2$/rGO hetero-structure is provided by high resolution STEM-EDS mapping. The HAADF image (Fig. 3d) shows the cross-section view of a WSe$_2$ nanoflake of 12 nm thickness composed of ~ 16 elementary nanosheets where the elementary nanosheets can be
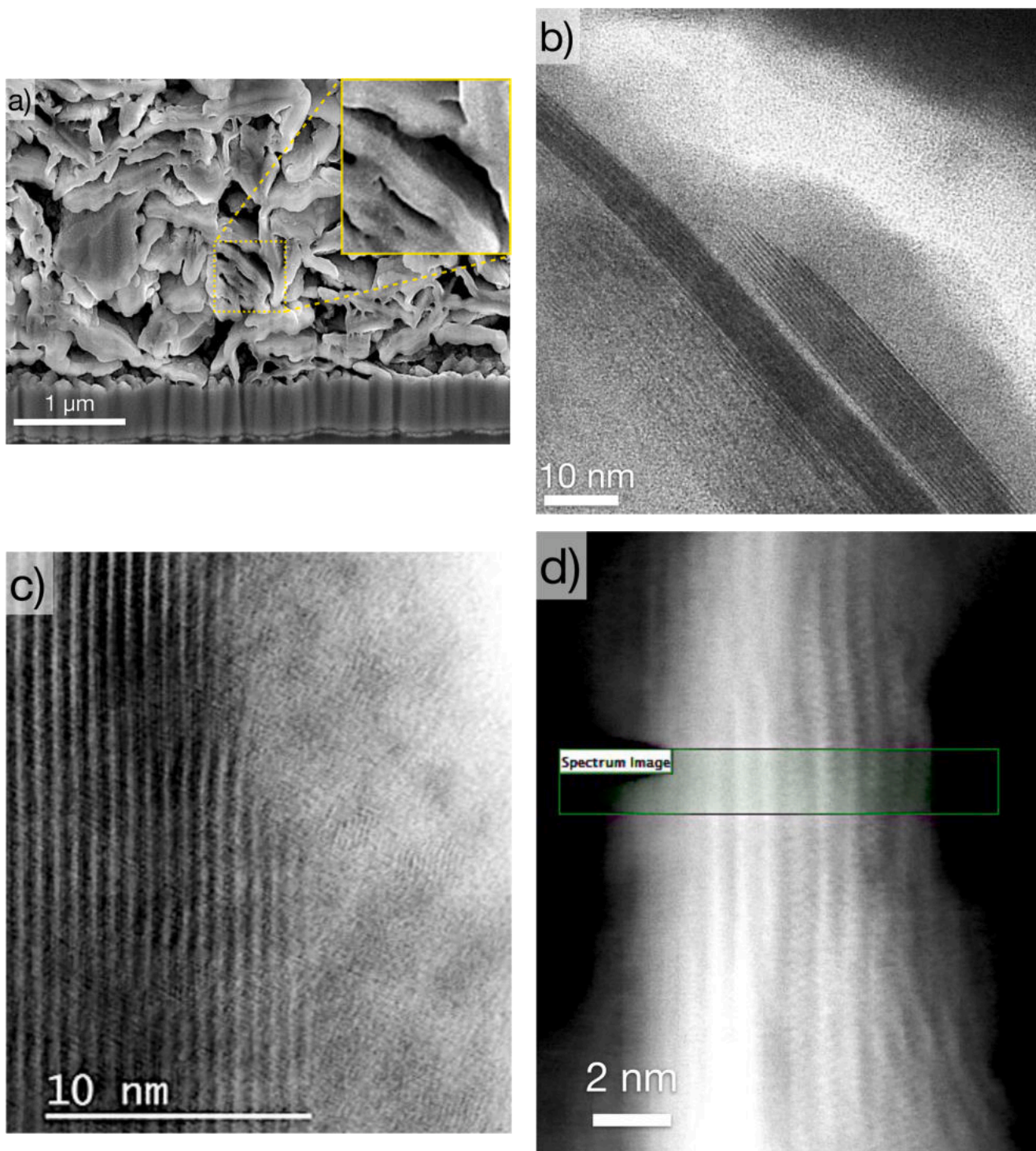
Fig. 3. Properties of co catalyst/WSe$_2$/rGO photo-electrodes. a) FIB-SEM cross section image showing an interconnected 3D porous assembly of WSe$_2$ anisotropic nanoflakes. Insert: Zoom showing presence of higher contrast linear domains all along the 120 nm thick co-catalyst/WSe$_2$ skeleton highlighting the stacking of 3 nanoflakes. b) High Resolution TEM image showing WSe$_2$ nanoflakes embedded in amorphous Mo$_x$S$_y$ co-catalyst. c) HRTEM image at nanometre scale demonstrating no degradation at the edge of a WSe$_2$ few-layer after co-catalyst deposition. d, e) Atomic-resolution HAADF-STEM image showing the detailed structure at the nanometer scale of the Mo$_x$S$_y$/WSe$_2$ layered hetero-structure. The ~5 nm thick WSe$_2$ nanoflake is sandwiched between an ultrathin, co-catalyst film of ~2 nm Mo$_x$S$_y$.

observed by contrast. As expected, STEM–EDS mapping reveals the presence of a ~ 12 nm core containing the W and Se elements. Although our co-self-assembly process favors the formation of 2D/2D, WSe$_2$/rGO planar interfaces, the coating of the WSe$_2$ nanoflake edges by rGO nanosheets has also been observed as shown from Carbon STEM–EDS mapping. This unambiguously demonstrates the presence of rGO in our

hetero-structures. In addition, STEM-EDS mapping analysis of Mo and S clearly shows the presence of Mo and S on the periphery of the WSe$_2$ nanoflake. Consistently with the post-deposition of an ultrathin (1 to 2 nm thick) Mo$_x$S$_y$ film onto the WSe$_2$/rGO nanostructured film, the WSe$_2$ nanoflake is sandwiched between two ultrathin layers of co-catalyst. This is the experimental evidence of the formation of the layered
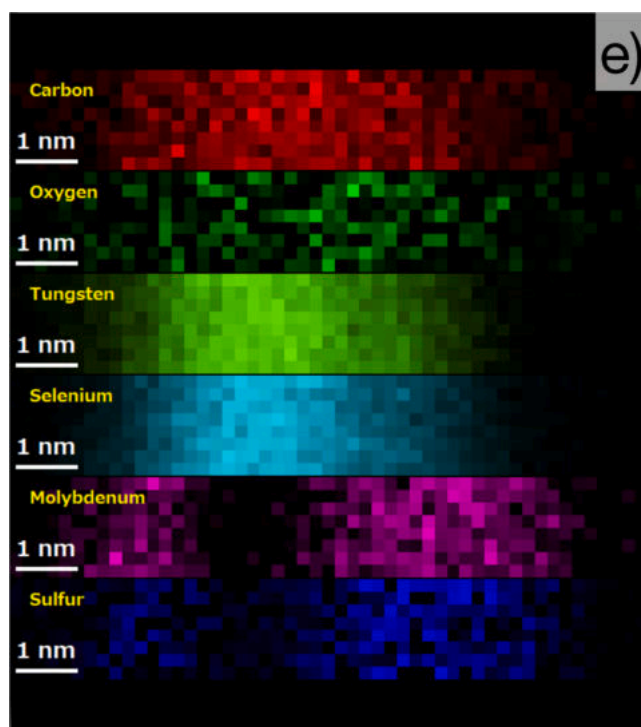
Fig. 3. (*continued*).

anisotropic hetero-structure spatially distributed according to the well-defined sequence $Mo_xS_y/WSe_2/rGO$ (Fig. 3d).

Note that the extension of rGO nanosheets outside the WSe_2 nano-flake has been also observed. Fig. S7 depicts another HAADF–STEM –EDS image of a 40 nm thick WSe_2 nanoflake together with an rGO nanosheet spreading out 60 nm from the WSe_2 nanoflake in a non-coiled conformation. All these results indicate the successful formation of a nanoporous skeleton formed from 120 nm thick, tri-layer hetero-structure building blocks composed of co-catalyst ultrathin film, WSe_2 nanoflake and rGO nanosheet.

Chemical composition of the ultrathin co-catalyst film was probed by XPS analysis. Because of the porous structure of the film and of the low average thickness ($e_{cc} < 10$ nm) of the co-catalyst film, XPS can be used to provide quantitative data of the chemical composition of the whole co-catalyst film as well as of the WSe_2 nanoflake surfaces. From the data extracted from the Mo 3d and the S 2p regions and using the assignments previously reported in the literature [42], an average value of S/Mo_{molar} 4.5 was determined for co-catalyst film withdrawn after the first hours of dip coating (5 h dip coating). Importantly, films displaying high photo-electrochemical performances and prepared at longer dip coating time (2x 16 h), exhibit a significant increase of the S/Mo ratio to S/Mo 5.2 (Fig. S3). The changes observed in the S/Mo ratio during the growth of the co-catalyst film probably result from different growth mechanisms. In a first step, deposition of thio-, oxo-thio- Mo complexes may be driven by adsorption energies on the bare WSe_2 while coordination–reticulation may later dictate the film growth process. The S/Mo value determined on our co-catalyst film compared with previously reported data [43,44] suggests the presence of $(Mo_2S_{12})^{2-}$ species in high proportions displaying a high catalytic activity [39] and high S/Mo ratio, in association with species displaying lower small S/Mo ratios such as $(MoOS_3)^{2-}$, $(Mo_2S_6O)^{2-}$ and $(MoS_4)^{2-}$.

3.4. Healing and optoelectronic properties of the co-catalyst ultrathin film

The healing properties of the co-catalyst film were first demonstrated by a photoluminescence investigation (Fig. 4a). PL measurements on the nanostr. catalyst-free/WSe_2/rGO films reveal no measurable luminescence as a consequence of the high concentration of electronically active surface defects usually present in these 2D materials. In contrast, despite bulk WSe_2 is known to display poor luminescence due to the indirect nature of its band gap, luminescence signals were clearly recorded for measurements performed on the $Mo_xS_y/WSe_2/rGO$ hetero-structures. Fig. 4a shows the wavelength shift of the PL emission peak-position from ~909 nm (1.36 eV) at 300 K to 780 nm (1.59 eV) at 4 K exciting the sample with the red line of a He-Ne laser (λ 632.8 nm) with a power of 500 μW. While the position of the PL peak of the room temperature photoluminescence could be interpreted as an envelope including mainly building blocks formed from several nanoflakes with an average thickness around 20–45 nm [45–46], the measurement of a sizeable PL intensity in these multilayer structures indicates the successful mitigation of defect-mediated non-radiative recombination.

In addition to the surface defects passivation, the co-catalyst film exhibits semi-conduction as demonstrated by UV–Vis spectroscopy (Fig. S8). From Mott-Schottky analysis, we have shown the n-type semi-conduction and determined the flat band potential of the co-catalyst film. Interestingly, in combination with the p-character of the WSe_2 nanoflakes (Fig. S8), the n-Mo sulfide co-catalyst ultrathin film was shown to build a beneficial p/n junction [47].

3.5. Increasing photo-electrochemical performances of the 2D photocatalyst by nanostructuration

Performance improvements resulting from the nanostructuration are clearly shown on the LSV curves (Fig. 4b) recorded on films prepared at r_{rGO} 0.15 using WSe_2/rGO co-textured powder in combination with a GO nanosheets post-addition. Compared with photocurrents recorded on reference photo-electrodes fabricated from drop-cast exfoliated-WSe_2 nanoflakes or nanostr. rGO-free/WSe_2 films, a remarkable large average photocurrent up to j 5 mA cm^{-2} at 0.2 V/NHE (on six replicate electrodes tested) in the range of the best values of the state of the art for photoactive 2D WSe_2 electrodes [23] was recorded under intermittent 1 sun illumination on the co-catalyst/WSe_2/rGO-hetero-structures. While no thickness dependence was observed for the rGO-free films, it is worth noting that the larger photocurrents were achieved on relatively thick
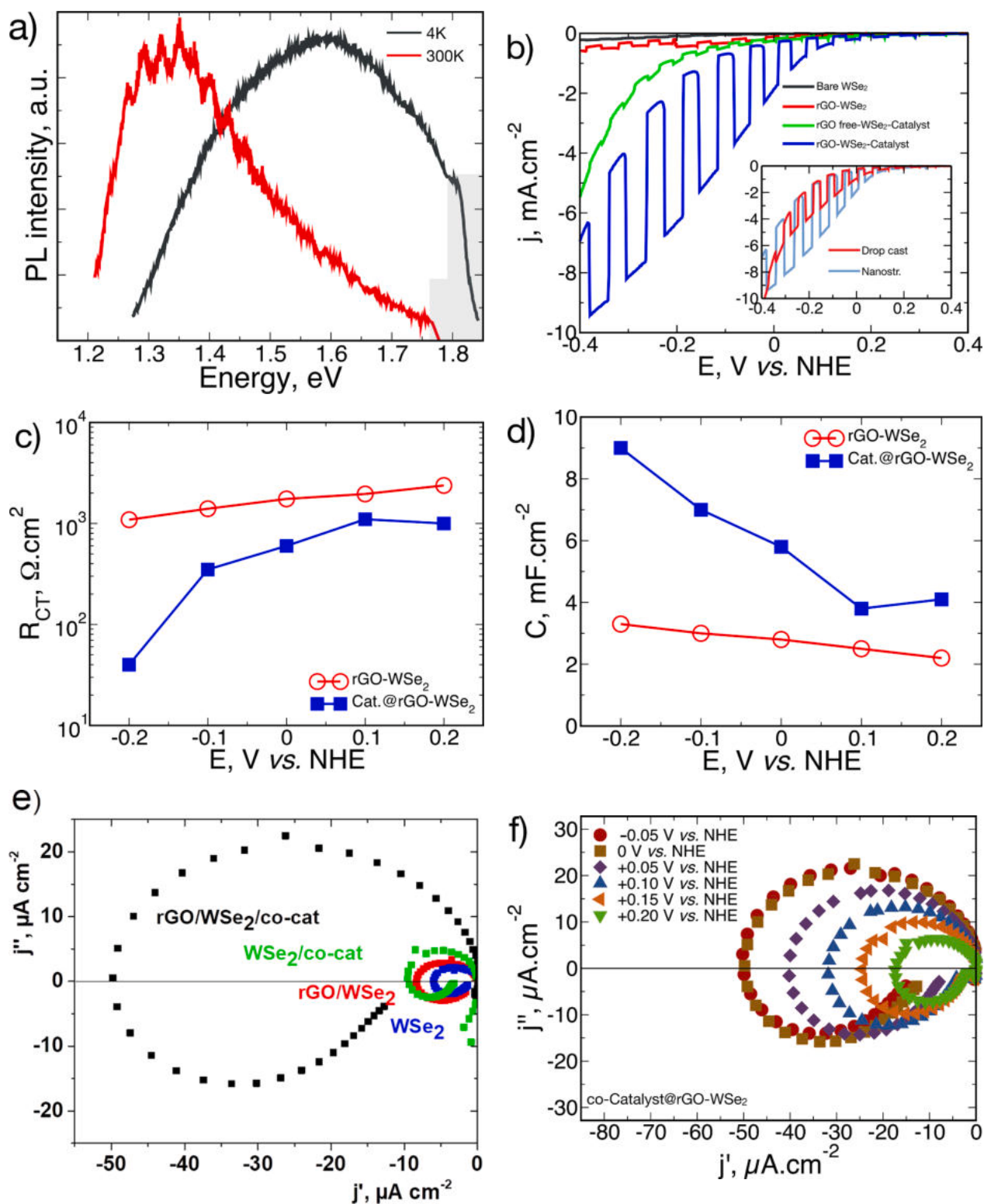
Fig. 4. Healing properties of the Mo_xS_y co-catalyst ultrathin film. a) Normalized PL of co-catalyst coated 2D WSe_2 photo-catalyst at 4 K and 300 K. b) LSV curve recorded on Mo_xS_y coated-nanostructured 2D WSe_2 photo-catalyst showing beneficial effect of nanostructuration. LSV curves on various reference photo-electrodes are given for comparison. Insert: LSV curves recorded on drop-cast (reference) and nanostructured co-catalyst coated/WSe_2 photo-electrodes. c) Charge transfer resistances R_{CT} and d) Capacitances fit from impedance responses of bare and co-catalyst coated WSe_2/rGO nanostructured photo-electrodes under illumination ($\lambda = 450$ nm), H_2SO_4 0.5 M, E = 0.1 V vs NHE. e) IMPS spectra of WSe_2-based photo-electrodes. E = 0.0 V vs NHE. Electrolyte H_2SO_4 0.5 M. $\lambda = 680$ nm. f) IMPS spectra of co-catalyst/WSe_2/rGO photo-electrode. Electrolyte H_2SO_4 0.5 M. $\lambda = 680$ nm. g) Recombination rate constants and h) Charge transfer rate constants for WSe_2-based photo-electrodes. Insert Fig. 4h: Zoom showing the increase of the charge transfer efficiency ($\eta_{ct} = k_{tr}/(k_{tr} + k_{rec})$) with polarization for co-catalyst coated/WSe_2 nanostructured photo-electrodes.
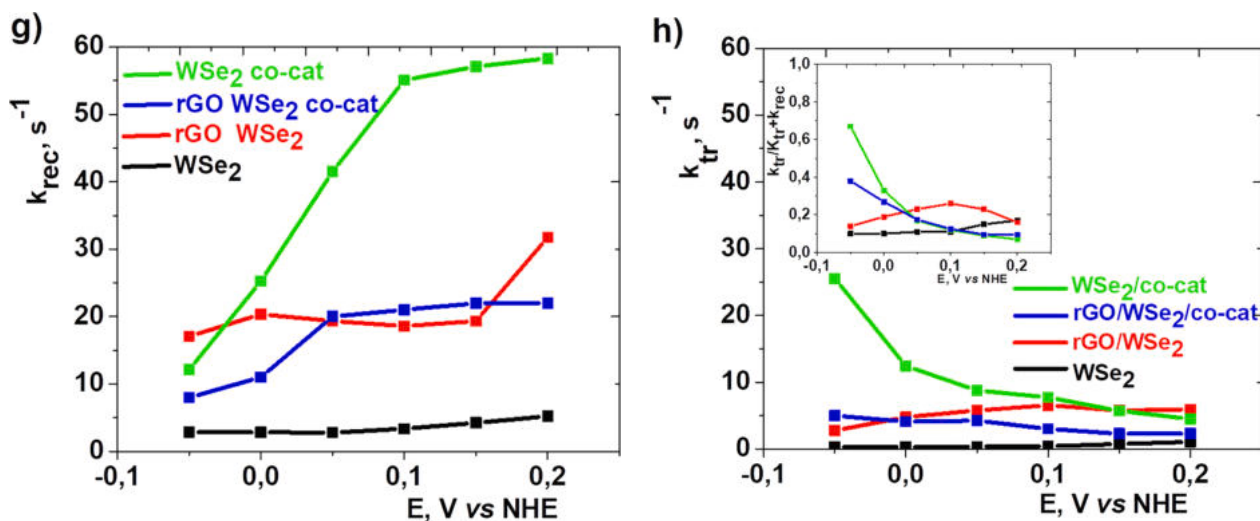
Fig. 4. (*continued*).

rGO/WSe$_2$/co-catalyst films (e 4 μm). Using the hetero-structuration strategy developed in this work, an optimal thickness of 4–5 μm was determined for our 2D nanoporous film yielding a 3-fold increase of the photocurrent density.

To demonstrate that the recorded photocurrent can be ascribed to the hydrogen formation, we have measured the real-time hydrogen evolution by gas chromatography (Fig. S9). Under continuous illumination, evolved H$_2$ gas was measured and compared to a Pt calibration curve. A Faradic yield around 95% was determined indicating proton reduction as the main reaction. Moreover, another important criterion is film stability. The chrono-amperometric behaviour of the catalyst/ WSe$_2$/rGO photo-electrode in 0.5 M H$_2$SO$_4$ is reported in Fig. S10 showing a nearly constant photocurrent observed under intermittent illumination demonstrating photo-electrode stability. In addition, no significant evolution was observed on the Raman spectra and TEM images recorded before and after HER testing. Although the co-catalyst film was formed from water-soluble Mo complexes, all these results are consistent with the formation of a partially well-reticulated, stable, co-catalyst film.

Incident-photon-to-current efficiency (IPCE) measurements were performed illuminating the photocathode using a set of high-power light emitting diodes (Fig. S11). The better IPCE value was determined at λ 760 nm with IPCE 13.2%. Although a better photon absorption is measured (Fig. S11) in the WSe$_2$ film over the wavelengths range 400–600 nm, as shown from the absorbance spectrum, lower IPCE values (10% at λ 515 nm) are determined at shorter wavelengths.

3.6. Effect of coverage ratio of the WSe$_2$ nanoflakes by rGO and MoxSy film on charge transfer and surface recombination

In addition to the LSV curves previously reported, an electrochemical impedance spectroscopy investigation (Fig. S12) under illumination (λ 450 nm) clearly reveals a lower charge transfer resistance along with a higher capacitance observed for the co-catalyst coated Mo$_x$S$_y$/WSe$_2$/ rGO photo-electrode compared with the bare one (Fig. 4c,d). For regular electrochemical processes under charge transfer control, the current is expected to vary exponentially with polarisation as observed for the bare sample (Fig. 4c). This is not the case for the coated one indicating a better charge separation and collection for this sample. Thus, in contrast to the regular exponential charge transfer dependence, the more efficient charge separation and longer minority charge carrier lifetime achieved for the coated Mo$_x$S$_y$/WSe$_2$/rGO sample allow the building up of a larger interface charge concentration and a higher capacitance (Fig. 4d). In addition to highlighting the increase of the effective charge

transfer surface site number, the capacitance increase can also be interpreted as a clear evidence of charge accumulation throughout the co-catalyst film. Indeed, several authors [37] have proposed that the capacitance increase could be assigned to the transfer of photo-generated charge carriers to the co-catalyst layer instead of being trapped in surface states of the photoactive material. In this interpretation, the charge carrier accumulation may imply a redox reaction involving the formation of intermediate species within the co-catalyst film such as unsaturated Mo(IV) sites which were furthermore previously identified as catalytically ready species. In addition, because these intermediates are subjected to recombination by oxidation, the observed increase of capacitance with polarization could be explained by hindered recombination with applied potential and band bending. Despite a partial coverage of the WSe$_2$ surface by the rGO nanosheet hindering the passivation of a proportion of in-plane surface defects, these results unambiguously demonstrate the beneficial effect of the co-catalyst film on improving the electron transfer as well as lowering the surface recombination.

Because the EIS investigation of the semiconductor/electrolyte interfaces involves a potential variation to modulate the whole reaction rate, this technique does not allow the deconvolution of the surface recombination and charge transfer processes. Better insight into the overall effective charge transfer resistance, i.e. deconvolution of the dark current and photocurrent, can be obtained by intensity modulated photocurrent spectroscopy (IMPS) [48] which allows the modulation of one reactant, i.e. the surface concentration of photo-generated carriers. Typical IMPS complex plots recorded in H$_2$SO$_4$ 0.5 M on non-coated and co-catalyst coated WSe$_2$/rGO nanostructured photo-electrodes are reported Fig. 4e,f and Fig. S12. The IMPS reference curves determined on drop-cast, non-coated and co-catalyst coated rGO-free, WSe$_2$ photo-electrodes are also given for comparison (Fig. S12-4). Except for the co-catalyst/WSe$_2$/rGO photo-electrode, all the photo-electrodes (WSe$_2$, WSe$_2$/rGO and co-catalyst/WSe$_2$) exhibit low frequency intercepts indicating, consistently with the photocurrents recorded on the LSV curves, a small fraction of the photocurrent injected into the electrolyte even at high cathodic potentials. Inspection of these IMPS curves also reveals a low dependence of the Nyquist curves with the applied potential for the WSe$_2$ photo-electrode. In contrast, a different behaviour is observed for the co-catalyst coated photo-electrodes. Particularly, the co-catalyst/WSe$_2$/rGO photo-electrode shows a much more potential dependent high frequency intercept together with a larger fraction of photo-generated electrons that reach the semiconductor/electrolyte interface. This notable difference, in agreement with the J –V curve (Fig. 4b) recorded on the nanostructured WSe$_2$/rGO photo-electrode

after co-catalyst deposition, probably results from the p/n junction formation following the co-catalyst deposition. Fig. 4g,h depicts the charge transfer (k_{tr}) and the recombination (k_{rec}) rates extracted from these plots. While a reasonable increase of k_{tr} values was determined with applied cathodic potentials for the non-coated, rGO-free, WSe$_2$ photo-electrode, deposition of the co-catalyst film yields as expected larger values of k_{tr} in the whole range of applied potentials. More important, IMPS data also clearly reveal that the addition of rGO significantly decreases the k_{tr} values. As previously observed from the HRTEM images, this could be attributed to the partial coverage of the WSe$_2$ nanoflake surfaces by the rGO nanosheets which diminishes the WSe$_2$ electrochemically active surface area. It is worth noting that this partial coverage of the photoactive WSe$_2$ surface by the rGO nanosheets was achieved for an incorporated r_{rGO} ratio (r_{rGO} 0.15) which corresponds to an equivalent surface coverage ~0.64. Note that this value is probably overestimated due to the presence of some rGO nanosheets of larger size extending out from the WSe$_2$ surface as shown from the TEM images (Fig. S7). Another key point extracted from these IMPS curves is the large values of k_{rec}. The larger values of k_{rec} observed for the co-catalyst coated WSe$_2$ photo-electrode probably arise both from the non-favourable band offset displayed by the co-catalyst band conduction level against the hydrogen evolution potential and from hindered hole transport to the back electrode. Consistently, a significant and favourable evolution of the k_{rec} values is observed either with applied cathodic potentials or after rGO insertion into the co-catalyst coated WSe$_2$ photo-electrode. Although the rGO-containing WSe$_2$/co-catalyst photo-electrode displays lower k_{rec} values compared with the rGO-free, WSe$_2$/co-catalyst photo-electrode, nearly similar charge transfer efficiency values (η_{CT} $k_{tr}/k_{tr} + k_{rec}$) were extracted from the IMPS curves.

Our results show that the partial coating of the WSe$_2$ photoactive material by the rGO nanosheets does not significantly alter the charge transfer efficiency of the WSe$_2$ photo-electrode. Despite the loss of photoactive surface area caused by the rGO shielding, the patch-like hetero-structuration strategy developed in this work proves to significantly increase the performances of the 2D photo-electrodes. This reveals that this loss is largely compensated by the surface area gain achieved by the mass loading increase resulting from the rGO addition.

3.7. Healing properties by thio-, oxo-thio-Mo monomers adsorption on WSe$_2$ edge defects

2D materials are known to display a large concentration of defects. These defects were mainly identified as in-plane (or internal) point defects including W or Se vacancies [49,50] especially for WSe$_2$ nanosheets of low thickness, i.e. e < 4 nm. For WSe$_2$ nanoflakes possessing a higher thickness (e 45–70 nm), edge defects become more important, making crucial interactions between edge defects and oxo-thio-Mo-complexes. To get better insights into the effect of MoxSy co-catalyst film on the passivation of the WSe$_2$ photo-electrode, adsorption energies of thio-, oxo-thio-Mo monomers $(MoOS_3)^{2-}$ and dimers $(Mo_2S_{12})^{2-}$ forming the co-catalyst layers were thus determined from DFT calculations. Because the edge defects were predominant in our nanoflakes, we first focused on adsorption modes (coordination and energies) of oxo-thio-Mo complexes on edge defects of a WSe$_2$ nanoflake.

Our model, built like any slab, from a 2H WSe$_2$ bulk system, see Supplementary Information for the computational details, exhibits few distinct adsorption sites, after a strong edge reconstruction, as it can be seen in Fig. S13. Indeed upon geometry optimization, the two edges presenting W-termination reconstruct themselves to always present Se-terminations.

To investigate the adsorption modes of the molecular complexes we have used their radical form, to avoid the complexity of studying charged species in periodic boundary conditions.

From these series of calculations, the $MoOS_3^{2-}$ complex was shown to display high adsorption energies towards the edge defects, around

4.83 to 5.51 eV depending on the coordination mode, while the adsorption energies for $(Mo_2S_{12})^{2-}$ complex are much weaker, from 0.66 eV to 0.84 eV. The most stable adsorption modes of $(Mo_2S_{12})^{2-}$ and $(MoOS_3)^{2-}$ complexes on these edge defects are given in Fig. 5. This suggests that passivation of edge defects probably results from the strong adsorption of the smaller molecular complexes on the edges. Moreover, these edge defects strongly adsorbed by the small thio-, oxo- thio-Mo-complexes probably act as nucleation sites thus favoring the formation of a continuous highly adherent coating of catalyst by chemical deposition.

With the findings of the most stable H-adsorption configurations for the two deposited Mo-based complexes, as given in Fig. 5, one can estimate their corresponding ΔG_H [51]. Interestingly the adsorption of an H species on an adsorbed $(MoOS_3)^{2-}$ gives a ΔG_H of 0.66 eV while it is 0.26 eV for $(Mo_2S_{12})^{2-}$. Although good catalytic activity for this Mo-dimer was previously reported in the literature in its free-standing form [37], our calculations show better catalytic performance of the $(Mo_2S_{12})^{2-}$ dimer -vs $(MoOS_3)^{2-}$ monomer- in their anchored configurations. Thus, DFT calculations clearly suggest that small complexes with low S/Mo ratio are strongly adsorbed and act as healing additives while polynuclear complexes such as $(Mo_2S_{12})^{2-}$ display catalytic activity. It is worth noting that these later complexes were shown by XPS to be localized at the film periphery in contact with the electrolyte.

Our patch-like hetero-structures exhibit 2D/2D, WSe$_2$/rGO interfaces achieved from a co-self-assembly process. Partial coverage of the photoactive WSe$_2$ nanoflake surfaces was tuned by use of rGO nanosheets of lower lateral size and control of the rGO addition ratio. As a result, the partial coating of the WSe$_2$ surface by the rGO nanosheets yields a proportion of non-healed, in-plane surface defects. Despite the presence of these non-healed, in-plane defects, our hetero-structuration strategy was proven to be efficient. This may result both from i) the relatively large thickness of the WSe$_2$ nanoflakes exhibiting a larger population of edge rather than in-plane defects ii) The favored injection of carrier into the electrolyte to achieve HER via these edge sites. Indeed, the photo-generated charge carriers flow preferentially through the in-plane direction as a result of its higher electronic conductivity [36,52]. Coating these edge-sites by a healing co-catalyst thus allows the passivation of the recombination centers while improving the charge transfer process on neighboring edge sites, yielding a significant increased photocurrent.

4. Conclusions

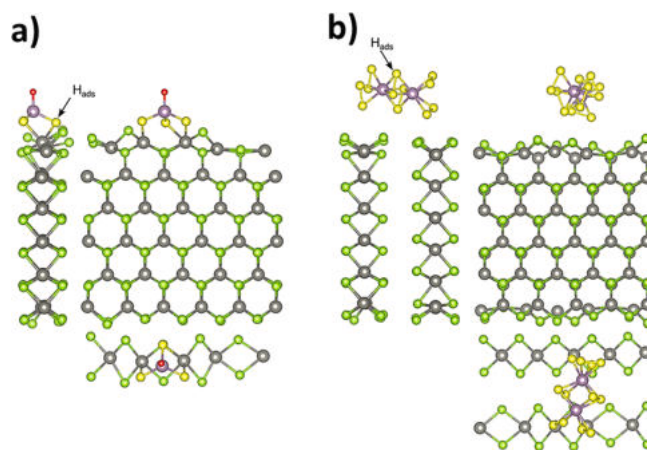A new nanostructured film composed of interconnected ultrathin,

Fig. 5. Side views (a) and top views (b) of the most stable adsorption modes for $(MoOS_3)^2$ in the left panel and $(Mo_2S_{12})^2$ species in the right panel. Se atoms are in reen, W in gray, S in yellow, O in red, when Mo atoms are in black. Black arrows correspond to the most stable coordination for a H atom.

layered hetero-structures made of WSe₂ nanoflakes, rGO nanosheets and a healing co-catalyst film is proposed. The WSe$_2$-based nanoporous network was prepared by co-self-assembly of WSe$_2$ nanoflakes, GO nanosheets of lower lateral size, and post-deposition of a co-catalyst ultrathin film. A resulting patch-like, layered, hetero-structure was achieved with partial coverages of the photoactive WSe$_2$ surface both by the rGO nanosheets and by the ultrathin co-catalyst film. Despite the partial shielding by the rGO nanosheets hindering the surface defects passivation by the healing co-catalyst film, the patch-like hetero-structuration strategy developed in this work proves to significantly increase the performances of 2D photo-electrodes. Good photoelectrochemical properties of WSe$_2$-based, patch-like hetero-structures were demonstrated with photocurrent densities up to 5 mA cm^{-2} for hydrogen generation. Future research efforts will be devoted to 2D TMDC films with lower thickness with the objective to increase surface area and photocurrent densities. We hope that this new strategy to improve charge transport properties in high surface area, layered hetero-structures will provide new and exciting opportunities to boost the performances of 2D photoactive materials for energy conversion.

Declaration of Competing Interest

The authors declare that they have no known competing financial interests or personal relationships that could have appeared to influence the work reported in this paper.

Acknowledgements

Appendix A. Supplementary data

Supplementary data to this article can be found online at https://doi.org/10.1016/j.cej.2021.130433.

References

[1] A. Heller, Hydrogen evolving solar cells, Science 223 (1984) 1141–1148.

[2] E.F. Osterloh, Inorganic nanostructures for photo-electrochemical and photocatalytic water splitting, Chem. Soc. Rev. 42 (6) (2013) 2294–2320.

[3] S.W. Boettcher, E.L. Warren, M.C. Putnam, E.A. Santori, D. Turner-Evans, M. D. Kelzenberg, M.G. Walter, J.R. McKone, B.S. Brunschwig, H.A. Atwater, N. S. Lewis, Photoelectrochemical hydrogen evolution using Si microwire arrays, J. Am. Chem. Soc. 133 (2011) 1216–1219.

[4] S.C. Warren, K. Voïtchovsky, H. Dotan, C.M. Leroy, M. Cornuz, F. Stellacci, C. Hébert, A. Rothschild, M. Gratzel, Identifying champion nanostructures for solar water-splitting, Nat. Mater. 12 (2013) 842–849.

[5] T.W. Kim, K.-S. Choi, Nanoporous BiVO₄ photoanodes with dual-layer oxygen evolution catalysts for solar water splitting, Science 343 (2014) 990–994.

[6] J. Barros Barbosa, P.L. Taberna, V. Bourdon, I.C. Gerber, R. Poteau, A. Balocchi, X. Marie, J. Esvan, P. Puech, A. Barnabé, L. Da Gama Fernandes Vieira, I.-T. Moraru, J.Y. Chane-Ching, Mo thio and oxo-thio molecular complexes film as self-healing catalyst for photocatalytic hydrogen evolution on 2D materials, Appl. Catal. B- Environ. 278 (2020), 119288.

[7] A. Heller, E. Aharon-Shalom, W.A. Bonner, B. Miller, Hydrogen-evolving semiconductor photocathodes. Nature of the junction and function of the platinum group metal catalyst, J. Am. Chem. Soc. 104 (1982) 6942–6948.

[8] M.S. Nasir, G. Yang, I. Ayub, S. Wang, L. Wang, X. Wang, W. Yan, S. Peng, S. Ramakarishna, Recent development in graphitic carbon nitride based photocatalysis for hydrogen generation, Appl. Catal. B- Environ. 257 (2019), 117855.

[9] Q.H. Wan, K. Kalantar-Zadeh, A. Kis, J.N. Coleman, M.S. Strano, Electronics and optoelectronics of two-dimensional transition metal dichalcogenides, Nat. Nanotechnol. 7 (2012) 699–712.

[10] P. Ganguly, M. Harb, Z. Cao, L. Cavallo, A. Breen, S. Dervin, D.D. Dionysiou, S. C. Pillai, 2D Nanomaterials for photocatalytic hydrogen production, ACS Energ. Lett. 4 (2019) 1687–1709.

[11] T. Su, Q. Shao, Z. Qin, Z. Guo, Z. Wu, Role of interfaces in two-dimensional photocatalyst for water splitting, ACS Catal. 8 (2018) 2253–2276.

[12] J. Jia, W. Sun, Q. Zhang, X. Zhang, X. Hu, E. Liu, J. Fan, Inter-plane heterojunctions within 2D/2D FeSe₂/g-C₃N₄ nanosheet semiconductors for photocatalytic hydrogen generation, Appl. Catal. B- Environ. 261 (2020), 118249.

[13] J. Xiong, J. Di, H. Li, Atomically thin 2D multinary nanosheets for energy-related photo electro-catalysis, Adv. Sci. 1800244 (2018).

[14] M.Q. Yang, Y.J. Xu, W.H. Lu, K.Y. Zeng, H. Zhu, Q.H. Xu, G.W. Ho, Self-surface charge exfoliation and electrostatically coordinated 2D hetero-layered hybrids, Nat. Commun. 8 (2017) 14224.

[15] M. Zhou, S. Wang, P. Yang, Z. Luo, R. Yuan, A.M. Asiri, M. Wakeel, X. Wang, Layered heterostructures of ultrathin polymeric carbon nitride and ZnIn₂S₄ nanosheets for photocatalytic CO₂ reduction, Chem. Eur. J. 24 (2018) 18529–18534.

[16] K.F. Mak, C. Lee, J. Hone, J. Shan, T.F. Heinz, Atomically thin MoS₂: a new direct-gap semiconductor, Phys. Rev. Lett. 105 (2010), 136805.

[17] J.R. McKone, A.P. Pieterick, H.B. Gray, N.S. Lewis, Hydrogen evolution from Pt/Ru-coated p-type WSe₂ photocathodes, J. Am. Chem. Soc. 135 (2013) 223–231.

[18] J. Kang, S. Tongay, J. Zhou, J. Li, J. Wu, Band offsets and heterostructures of two-dimensional semiconductors, Appl. Phys. Lett. 102 (2013), 012111.

[19] H.L. Zhuang, R.G. Hennig, Computational search for single-layer transition-metal dichalcogenide photocatalysts, J. Phys. Chem. C 117 (2013) 20440–20445.

[20] C.R. Cabrera, H.D. Abruna, Synthesis and photoelectrochemistry of polycrystalline thin films of p-WSe₂, p-WS₂ and p-MoSe₂, J. Electrochem. Soc. 135 (6) (1988) 1436–1442.

[21] J. Hong, Z. Hu, M. Probert, K. Li, D. Lv, X. Yang, L. Gu, N. Mao, Q. Feng, L. Xie, J. Zhang, D. Wu, Z. Zhang, C. Jin, W. Ji, X. Zhang, J. Yuan, Z. Zhang, Exploring atomic defects in molybdenum disulphide monolayers, Nat. Commun. 6 (2015) 6293.

[22] M. Amani, D.H. Lien, D. Kiriya, J. Xiao, A. Azcatl, J. Noh, S.R. Madhvapathy, R. Addou, K.C. Santosh, M. Dubey, K. Cho, R.M. Wallace, S.C. Lee, J.H. He, J. W. Ager, X. Zhang, E. Yablonovitch, A. Javey, Near-unity photoluminescence quantum yield in MoS₂, Science 350 (2015) 1065–1068.

[23] X. Yu, N. Guijarro, M. Johnson, K. Sivula, Defect mitigation of solution-processed 2D WSe₂ nanoflakes for solar-to-hydrogen conversion, Nano Lett. 18 (2018) 215–222.

[24] R. Liu, Z. Zheng, J. Spurgeon, X. Yang, Enhanced photoelectrochemical water-splitting performance of semiconductors by surface passivation layers, Energ. Environ. Sci. 7 (2014) 2504.

[25] V. Agarwala, N. Varghesea, S. Dasguptaa, A.K. Soodb, K. Chatterjeea, Engineering a 3D MoS₂ foam using keratin exfoliated nanosheets, Chem. Eng. J. 374 (2019) 254–262.

[26] M.H. Wahid, X. Chen, C.T. Gibson, C.L. Raston, Amphiphilic graphene oxide stabilisation of hexagonal BN and MoS₂ sheets, Chem. Commun. 51 (2015) 11709.

[27] J.N. Coleman, M. Lotya, A.O. Neill, S.D. Bergin, P.J. King, U. Khan, K. Young, A. Gaucher, S. De, R.J. Smith, I.V. Shvets, S.K. Arora, G. Stanton, H.Y. Kim, K. Lee, G.T. Kim, G.S. Duesberg, T. Hallam, J.J. Boland, J.J. Wang, J.F. Donegan, J. C. Grunlan, G. Moriarty, A. Shmeliov, R.J. Nicholls, J.M. Perkins, E.M. Grieveson, K. Theuwissen, D.W. McComb, P.D. Nellist, V. Nicolosi, Two-dimensional nanosheets produced by liquid exfoliation of layered materials, Science 331 (2011) 568.

[28] R.H. Arntson, P.X. Dickson, G. Tunell, Stibnite (Sb₂S₃) solubility in sodium sulfide solutions, Science 153 (1966) 1673–1674.

[29] M.V. Kovalenko, M. Scheele, D.V. Talapin, Colloidal nanocrystals with molecular metal chalcogenide surface ligands, Science 324 (2009) 1417–1420.

[30] M.V. Kovalenko, M.I. Bodnarchuk, J. Zaumseil, J.-S. Lee, D.V. Talapin, Expanding the chemical versatility of colloidal nanocrystals capped with molecular metal chalcogenide ligands, J. Am. Chem. Soc. 132 (2010) 10085–10092.

[31] Y. Wang, X. Di, X. Gao, X. Wu, P. Wang, Rational construction of Co@C polyhedrons covalently-grafted on magnetic graphene as a superior microwave absorber, J. Alloys Compd. 843 (2020) 156031–156042.

[32] Y. Wang, X. Di, X. Gao, X. Wu, Design of MOF-derived hierarchical Co@C@RGO composite with controllable heterogeneous interfaces as a high-efficiency microwave absorbent, Nanotechnology 31 (2020), 395710.

[33] P. Biloen, G. Pott, X-ray photoelectron spectroscopy study of supported tungsten oxide, J. Catal. 30 (1973) 169–174.

[34] W. Jaegermann, D. Schmeisser, Reactivity of layer type transition metal l chalcogenides towards oxidation, Surf. Sci. 165 (1986) 143–160.

[35] W.H. Hall, X-ray line broadening in metals, Proc. Phys. Soc. Sect. A 62 (11) (1949) 741–743.

[36] Y. Jung, J. Shen, Y. Liu, J.M. Woods, Y. Sun, J.J. Cha, Metal seed layer thickness-induced transition from vertical to horizontal growth of MoS₂ and WS₂, Nano Lett. 14 (2014) 6842–6849.

[37] B. Klahr, S. Gimenez, F. Fabregat-Santiago, J. Bisquert, T.W. Hamann, Photoelectrochemical and impedance spectroscopic investigation of water oxidation with "Co–Pi"-coated hematite electrodes, J. Am. Chem. Soc. 134 (2012) 16693–16700.

[38] J.H. Kim, S. Han, Y. Hyun Jo, Y. Bak, J.S. Lee, A precious metal-free solar water splitting cell with a bifunctional cobalt phosphide electrocatalyst and doubly promoted bismuth vanadate photoanode, J. Mater. Chem. A 6 (2018) 1266–1274.

[39] Z. Huang, W. Luo, L. Ma, M. Yu, X. Ren, M. He, S. Polen, K. Click, B. Garrett, J. Lu, K. Amine, C. Hadad, W. Chen, A. Asthagiri, Y. Wu, Dimeric [Mo₂S₁₂]²⁻ cluster: a molecular analogue of MoS₂ edges for superior hydrogen-evolution electrocatalysis, Angew. Chem. Int. Ed. 54 (2015) 15181–15185.

[40] J. McAllister, N.A.G. Bandeira, J.C. McGlynn, A.Y. Ganin, Y.-F. Song, C. Bo, H. N. Miras, Tuning and mechanistic insights of metal chalcogenide molecular catalysts for the hydrogen evolution reaction, Nat. commun. 10 (370) (2019) 1–10.

[41] Y. Li, A. Chernikov, X. Zhang, A. Rigosi, H.M. Hill, A.M. van der Zande, D. A. Chenet, E.-M. Shih, J. Hone, T.F. Heinz, Measurement of the optical dielectric function of transition metal dichalcogenide monolayers: MoS₂, MoSe₂, WS₂ and WSe₂, Phys. Rev. B 90 (2014), 205422.

[42] J. Kibsgaard, T.F. Jaramillo, F. Besenbacher, Building an appropriate active site motif into a hydrogen evolution catalyst with thiomolybdate $[Mo_3S_{13}]^{2-}$ clusters, Nat. Chem. 6 (2014) 248–253.

[43] C.G. Morales-Guio, X. Hu, Amorphous molybdenum sulfides as hydrogen evolution catalysts, Acc. Chem. Res. 47 (2014) 2671–2681.

[44] P.D. Tran, T.V. Tran, M. Orio, S. Torelli, Q.D. Truong, K. Nayuki, Y. Sasaki, S. Y. Chiam, R. Yi, I. Honma, J. Barber, V. Artero, Coordination polymer structure and revisited hydrogen evolution catalytic mechanism for amorphous molybdenum sulfide, Nat. Mater. 15 (2016) 640–647.

[45] A. Arora, M. Koperski, K. Nogajewski, J. Marcus, Excitonic resonances in thin films of WSe_2: from monolayer to bulk material, Nanoscale 7 (2015) 10421–10429.

[46] Y. Li, J. Shi, H. Chen, R. Wang, Y. Mi, C. Zhang, W. Du, S. Zhang, Z. Liu, Q. Zhang, X. Qiu, H. Xu, W. Liu, Y. Liu, X. Liu, The Auger process in multilayer WSe_2 crystals, Nanoscale 10 (2018) 17585.

[47] M. Zhong, T. Hisatomi, Y. Kuang, J. Zhao, M. Liu, A. Iwase, Q. Jia, H. Nishiyama, T. Minegishi, M. Nakabayashi, N. Shibata, R. Niishiro, C. Katayama, H. Shibano, M. Katayama, A. Kudo, T. Yamada, K. Domen, Surface modification of CoOx loaded $BiVO_4$ photoanodes with Ultrathin p-Type NiO layers for improved solar water oxidation, J. Am. Chem. Soc. 137 (2015) 5053–5060.

[48] E.A. Ponomarev, L.M. Peter, A generalized theory of Intensity Modulated Photocurrent Spectroscopy (IMPS), J. Electroanal. Chem. 396 (1995) 219–225.

[49] S. Zhang, C.-G. Wang, M.-Y. Li, D. Huang, L.-J. Li, W. Ji, S. Wu, Defect structure of localized excitons in a WSe_2 monolayer, Phys. Rev. Lett. 119 (046101) (2017) 1–6.

[50] Y. Guo, D. Liu, J. Robertson, Chalcogen vacancies in monolayer transition metal dichalcogenides and Fermi level pinning at contacts, Appl. Phys. Lett. 106 (2015), 173106.

[51] J.K. Nørskov, T. Bligaard, A. Logadottir, J.R. Kitchin, J.G. Chen, S. Pandelov, U. Stimming, Trends in the Exchange current for hydrogen evolution, J. Electrochem. Soc. 152 (3) (2005) J23–6.

[52] W. Kautek, Electronic mobility anisotropy of layered semiconductors: transversal photoconductivity measurements at n-$MoSe_2$, J. Phys. C: Solid State Phys. 15 (1982) L519.

Patch-like, Two Dimensional WSe$_2$-based Hetero-structures Activated by a Healing Catalyst for H$_2$ Photocatalytic Generation.

P.L. Taberna, J. Barros Barbosa, A. Balocchi, I. Gerber, K. Urita, A. Barnabe, X. Marie, J.Y. Chane-Ching*.

Email:chane.jy@gmail.com

Supporting information.

Figures.

Figure S1: $Sn_xSb_yS_z$ template, GO nanosheets and WSe_2 nanoflakes properties.

In preliminary experiments, GO nanosheets of average size L= 80-120 nm, were selected consistently both with the WSe_2 nanoflake lateral size, (L= 200 -1000 nm) and template average size (D= 60 nm).
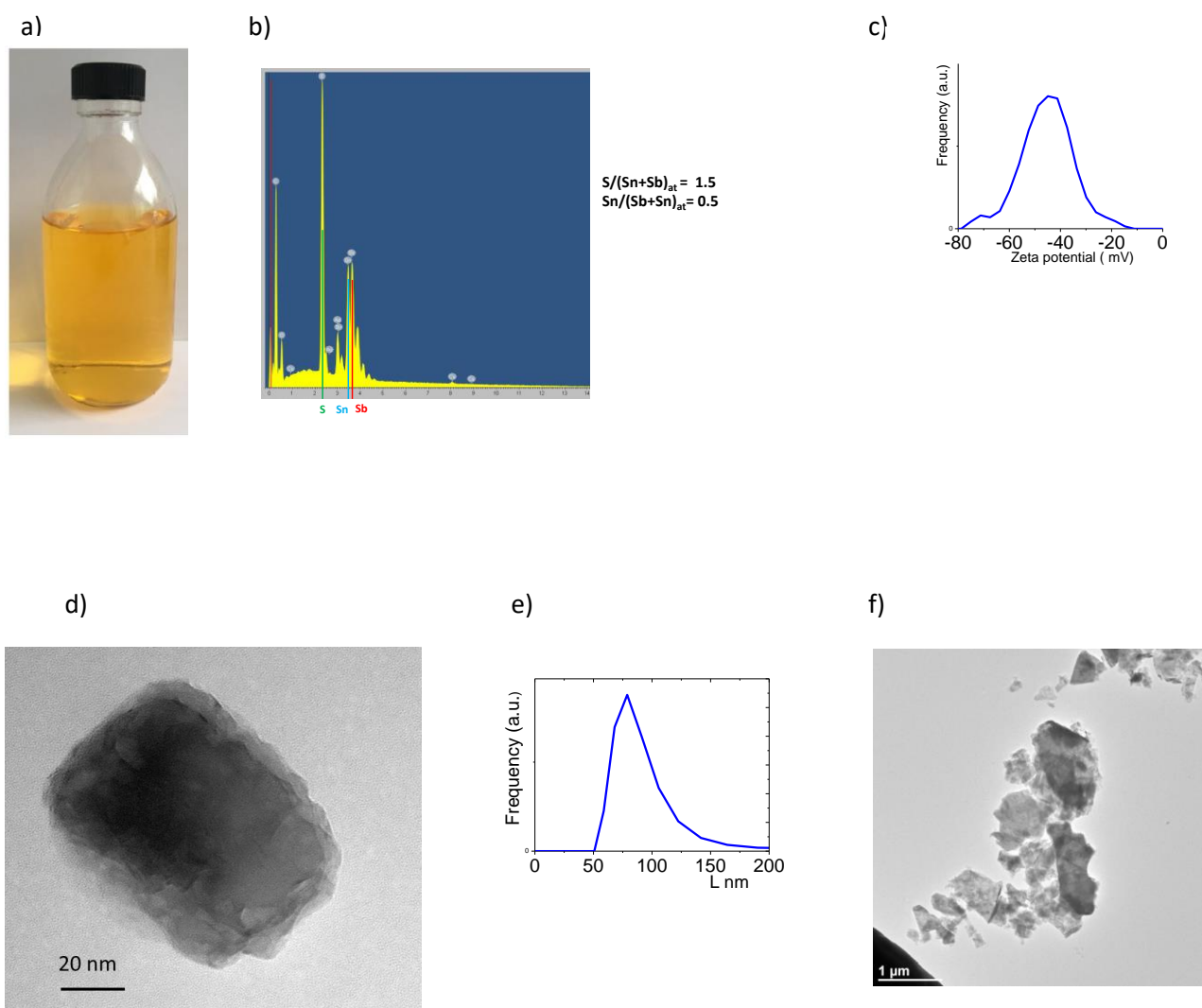
Figure S1: $Sn_{0.5}Sb_{0.5}S_{1.5}$ template, WSe_2 nanoflakes and GO nanosheets properties. a) Photograph of an aqueous colloidal dispersion of $Sn_{0.5}Sb_{0.5}S_{1.5}$. b) Energy Dispersive Spectroscopy performed on $Sn_{0.5}Sb_{0.5}S_{1.5}$ dried at 80 °C. c) Zeta potential of $Sn_{0.5}Sb_{0.5}S_{1.5}$ colloids in H_2O, pH 9, showing a negative surface charge. d) Typical TEM image of GO nanosheets selected at 15 300 rpm. e) Size distribution of exfoliated GO nanosheets showing a mean lateral size of ~ 80 nm. f) Typical TEM image of exfoliated WSe_2 nanoflakes after selection at 800 rpm showing hetero-disperse size distribution of the nanoflakes.

Figure S2: Pore volume and surface area characteristics of nanostructured WSe₂ and WSe₂ /rGO powders.

a)   b)
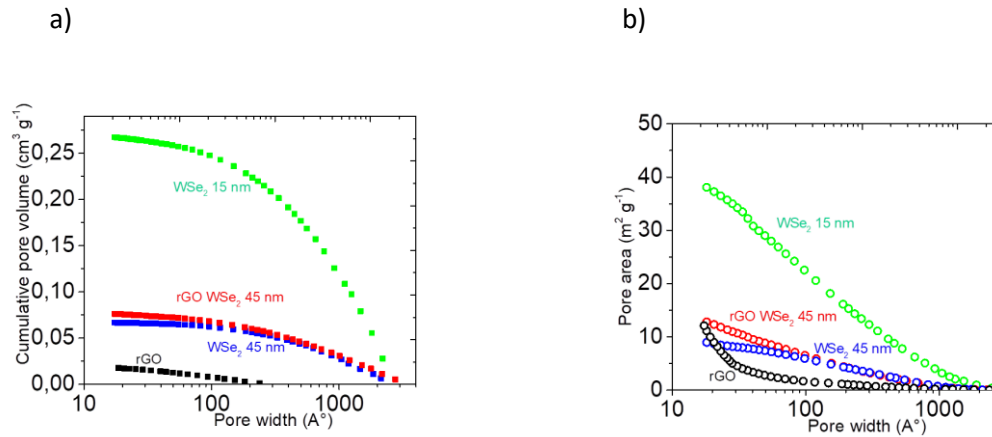
Figure S2: a) Pore volume and b) pore area characteristics of nanostructured WSe₂ and rGO-WSe₂ powders self-assembled from WSe₂ nanoflakes selected at various ultracentrifugation speeds. i) Nanostructured WSe₂ powder, selection at 5000 rpm, nanoflake thickness ~ 15 nm. ii) Nanostructured WSe₂ powder, selection at 800 rpm, nanoflake thickness ~ 45 nm. iii) Nanostructured rGO-WSe₂ powder, WSe₂ nanoflake thickness ~ 45 nm. Pore volume and pore area characteristics of textured rGO powder, self-assembled in similar conditions were also given for reference. The higher pore volume and pore area values observed on WSe₂ -containing textured powders compared with pure rGO textured powder highlight better interactions between WSe₂ surface and the ($Sn_{0.5}Sb_{0.5}S_y$) colloids template.

As expected, higher pore volume and pore area are observed for textured WSe₂ powders prepared from WSe₂ nanoflakes of lower thickness. Note that an experimental BET surface area value of 7 m^2 g^{-1} was measured on nanostructured WSe₂ powder prepared from nanoflakes exhibiting a thickness of 45 nm.
This experimental BET surface value is consistent with the surface area of 6 -7 m^2 g^{-1}, calculated for nanoflakes exhibiting a thickness e, e= 45 nm.
S= N * 2 (L l + L e + l e)   N= number of nanoflakes,   L, l, e nanoflake dimensions
S= M * 2 (L l + L e + l e) / ρ L l e ρ= WSe₂ density, M= nanoflakes mass
S= 2 M (1/e + 1/l + 1/L) / ρ
e= 45 nm   L= 500 nm, l= 200 nm, ρ= 9.32 g/cm^3
S= 6.2 m^2 g^{-1}

Surface coverage ratio of the WSe₂ nanoflakes by rGO nanosheets.

$r_{rGO\ molar}$	wt% rGO	σ coverage ratio
0.05	0.18	0.21
0.10	0.36	0.43
0.15	0.54	0.64
0.20	0.72	0.85
0.30	1.08	1.28

r_{rGO} = rGO/(WSe₂ + rGO)$_{molar}$

σ= Surface coverage ratio of the WSe_2 nanoflakes by rGO nanosheets

σ = r_{rGO} N_{rGO} s_{rGO} / N_{WSe2} s_{WSe2} where N_{rGO} N_{WSe2} denote respectively the number of rGO nanosheets and WSe_2 nanoflakes and, s_{rGO} and s_{WSe2} denote respectively the surface area of one rGO nanosheet and one WSe_2 nanoflake

σ= r_{rGO} Mw_{rGO} ρ_{WSe2} e_{WSe2} / 2 Mw_{WSe2} ρ_{rGO} e_{rGO} = 4.3 r_{rGO}

(e_{WSe2} = 45 nm e_{rGO} = 1 nm ρ_{WSe2} = 9.32 g cm^{-3} ρ_{rGO} = 2 g cm^{-3})

Figure S3: XPS characteristics of a high performance MoxSy/ WSe₂/rGO   FTO photo-electrode.

a)
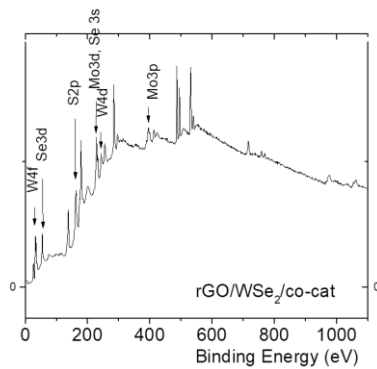
b)
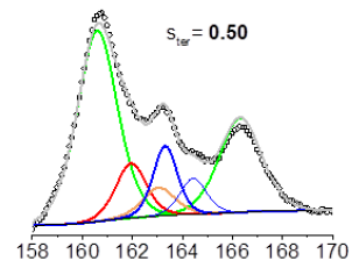
c)
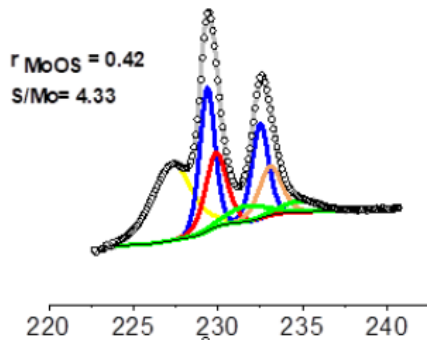
d)
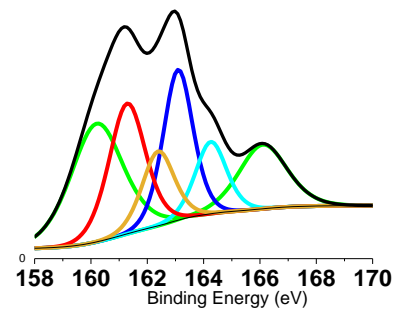
e)
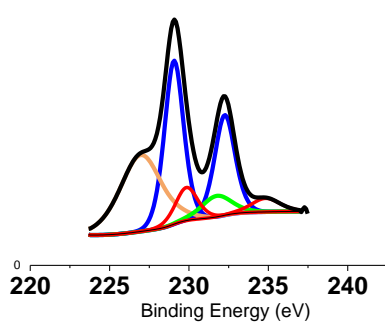
f)
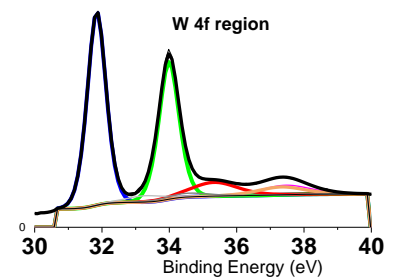
Figure S3: XPS curves recorded on a high performance co-catalyst-rGO-WSe$_2$ nanostructured film (j= 5 mA cm^{-2} was recorded at - 0.2 V vs NHE in 0.5 M H$_2$SO$_4$). The co-textured rGO-WSe$_2$ powder was prepared by co-self-assembly using WSe$_2$ solvent-exfoliated nanoflakes selected at 800 rpm. The co-catalyst films were deposited as follows.

a) XPS survey spectrum of high performance Co-catalyst/WSe$_2$/rGO film.

b) Co-catalyst film dip coated 4h. XPS core-level spectra and deconvolution into S 2p and Se 3p contributions. Se 3p 3/2 (BE= 160.0 eV, Green). S 2p 3/2 peaks having binding energies of 161.3 eV, and 163.1 eV were respectively assigned to terminal S$_2^{2-}$ and bridging S$_2^{2-}$. The terminal S$_2^{2-}$ ratio was determined, S$_{ter}$ /(S$_{ter}$ + S$_{br}$)= 0.50.

c) Co-catalyst film dip coated 4h. XPS core-level spectra and deconvolution into Mo 3d, Se 3s and S 2s contributions. Fitting envelopes attributed to the Mo(IV) ion in MoS$_2$ are Mo 3d 5/2 (BE= 229.06 eV, Blue), Mo(IV) in Mo oxysulfide complexes, MoO$_y$S$_z$, (BE= 231.74 eV, red). The S/Mo ratio was determined from data extracted from the Mo(IV) 3d and S 2s regions, S/Mo= 4.33.

d) Co-catalyst film dip-coated 2x 16 h. XPS core-level spectra and deconvolution into S 2p and Se 3p contributions. The terminal S$_2^{2-}$ ratio was determined, S$_{ter}$ /(S$_{ter}$ + S$_{br}$)= 0.51.

e) Co-catalyst film dip coated 2x 16 h. XPS core-level spectra and deconvolution into Mo(IV) 3d, Se 3s and S 2s contributions. The S/Mo ratio was determined from data extracted from the Mo(IV) 3d and S 2s regions, S/Mo= 5.18.

f) Co-catalyst film dip coated 2x 16 h. XPS spectra of W(IV) 4f core level of the sample. The solid lines are experimental data. The red / orange and blue / blue colored lines are Lorentzian fits for the peaks of WSe$_2$ and W(IV)O$_x$ respectively.

X-ray Photoelectron Spectroscopy was performed on a ThermoScientific K-Alpha system with monochromatic Al Kα (hv = 1486.6 eV). All the XPS spectra were calibrated with C 1s at 284.6 eV (± 0.1eV).

Figure S4: Structure properties of nanostructured WSe$_2$ photo electrodes.

Crystallographic information on rGO-WSe$_2$-MoxSy films deposited on FTO/ Glass substrates was obtained on a Brucker AXS D4 diffractometer operating in the Bragg configuration, using a monochromatized CuKα radiation (λ= 1.540596 Å). Diffraction patterns were collected from 2θ = 10 to 80 ° at a scanning rate of 0.69° per minute with a step size of 0.01°.
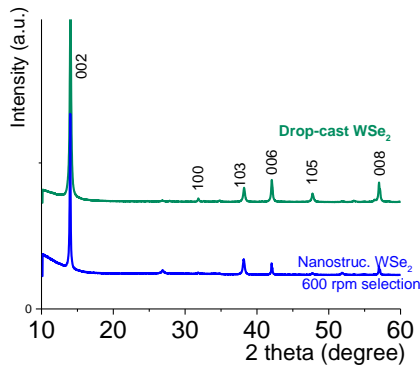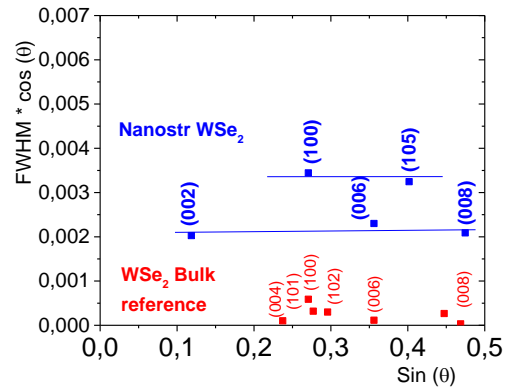
Figure S4: a) Structure properties of nanostructured WSe₂ photo electrodes. The diffractogram of the drop-cast WSe₂ sample was given for comparison. Larger preferential orientation along the c-axis can be observed for the drop-cast sample showing a larger intensity peak ratio, $I_{(006)}$/ $I_{(103)}$ for the drop-cast sample, $I_{(006)}$ and $I_{(103)}$ denoting peak intensity of the (006) and (103) diffraction lines. In contrast, loss of preferential orientation along the c-axis is consistent with the random orientation of the WSe₂ nanoflakes as observed on the FIB- SEM cross-section for the nanostructured film. b) Williamson–Hall plot* of nanostructured WSe₂ film prepared from nanoflakes selected at 800 rpm. Data extracted from the WSe₂ bulk reference sample diffraction pattern are given for comparison. Details of the calculations are given in Table S4.

*Using the Williamson-Hall model, for a given reflection, the full width at half maximum intensity (FWHM) can be expressed as the convolution

FWHM = FWHM$_{equip}$ + FWHM $_{sample}$

Where FWHM $_{sample}$ corresponds to diffraction line profiles broadening in relation to a control sample, due to size and strain effects and FWHM$_{equip}$ denotes modification of diffraction line profiles due to instrumental effects. For our equipment, FWHM $_{equip.}$ = 0.085

FWHM = FWHM$_{equip}$ + FWHM $_{sample, size}$ + FWHM $_{sample, strain}$

$\cos \theta$ (FWHM - FWHM $_{equip.}$) = 0.9 λ / t + 2 Δd/d $\sin \theta$ (1)

To determine t, diffracting domain size from equation (1), we plot $\cos \theta$ (FWHM - FWHM $_{equip.}$) = f ($\sin \theta$). t was extracted from the Y axis intercept (0.9 λ / t).

Bulk WSe₂ reference sample

h k l	2θ	Sin θ	FWHM	FWHM _equip._	Δ FWHM * cos θ
002	13,624	0,118			
004	27,463	0,237	0,091	0,085	0,00010
100	31,41	0,271	0,12	0,085	0,00059
101	32,174	0,277	0,104	0,085	0,00032
102	34,408	0,296	0,103	0,085	0,00030
103	37,805	0,324	0,084	0,085	
006	41,707	0,356	0,092	0,085	0,00011
105	47,363	0,402	0,09	0,085	0,00008
106	53,136	0,447	0,102	0,085	0,00026
110	55,901	0,469	0,087	0,085	0.00003
008	56,672	0,475	0,012	0,085	

Nanostructured WSe₂ sample

h k l	2θ	Sin θ	FWHM	FWHM _equip_	Δ FWHM * cos θ
002	13,624	0,118	0,202	0,085	0,00202
004	27,463	0,237	0,39	0,085	
100	31,41	0,271	0,29	0,085	0,00344
101	32,174	0,277			
102	34,408	0,296			
103	37,805	0,324	0,409	0,085	0,00535
006	41,707	0,356	0,226	0,085	0,00230
105	47,363	0,402	0,288	0,085	0,00324
106	53,136	0,447			
110	55,901	0,469			
008	56,672	0,475	0,221	0,085	0,00209

Table S4: ΔFWHM * cosθ for nanostructured WSe₂ sample and bulk WSe₂ reference sample

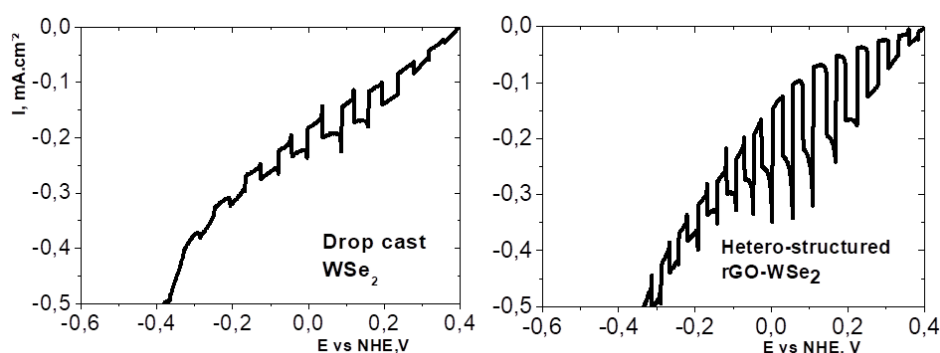Figure S5: Typical LSV curve on hetero-structured rGO/WSe₂ photo-electrode. r_{rGO}= 0.15. LSV curve on a drop-cast WSe₂ photo-electrode is given for reference. Electrolyte H_2SO_4 0.5 M

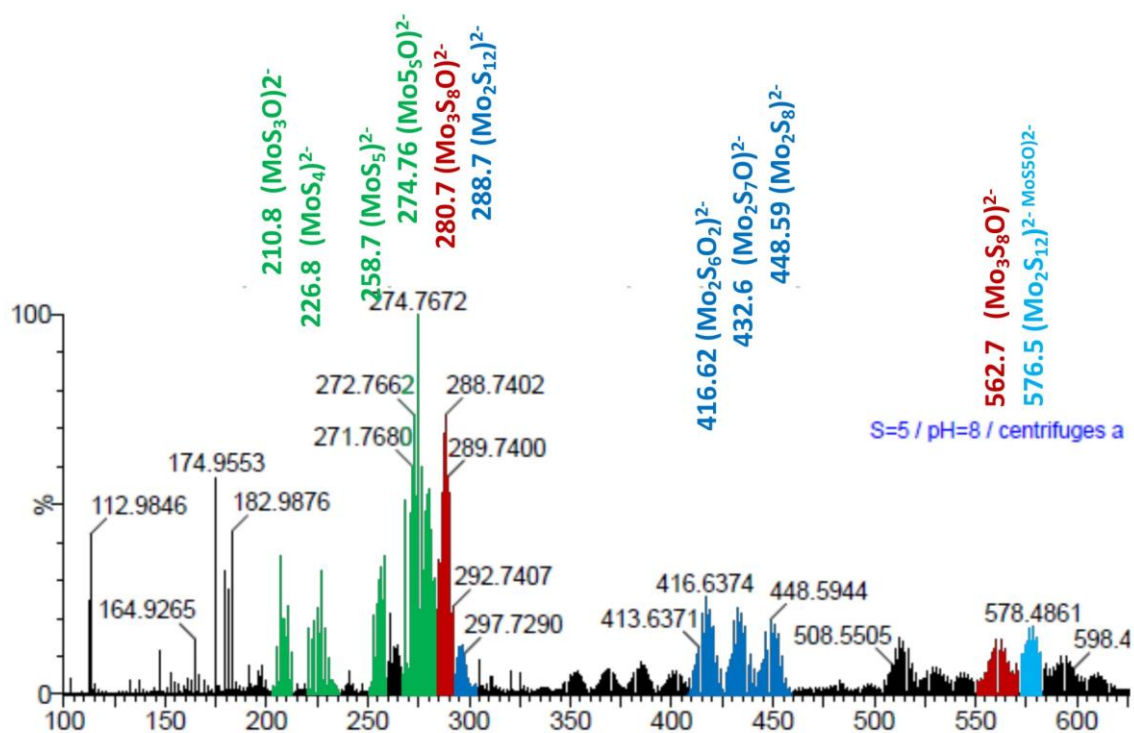*Figure S6: Electrospray Ionization Mass Spectrometry (ESI-MS) of thio-, oxo-thio- Mo complexes aqueous solution.*

Figure S6: Electrospray Ionization Mass Spectrometry (ESI-MS) spectrum of thio-, oxo-thio-Mo complexes aqueous solution pH 9, S/Mo= 5 showing presence of Mo monomers, dimers and trimers. Spectra were recorded using a Xevo G2 Q Tof MS instrument equipped with an electrospray (ESI) source supplied by Waters. Data were processed using the Masslynx 4.1 software. Fragmentation was minimized by setting cone voltage at 20 V. The MS data were collected in negative ion mode. The thio-, oxo-thio- Mo complexes aqueous solutions (0.01 M Mo) were diluted x20 before introduction into the MS. The spectrometer was calibrated to give a precision of 3.0 ppm in the region 100–2000 m/z.

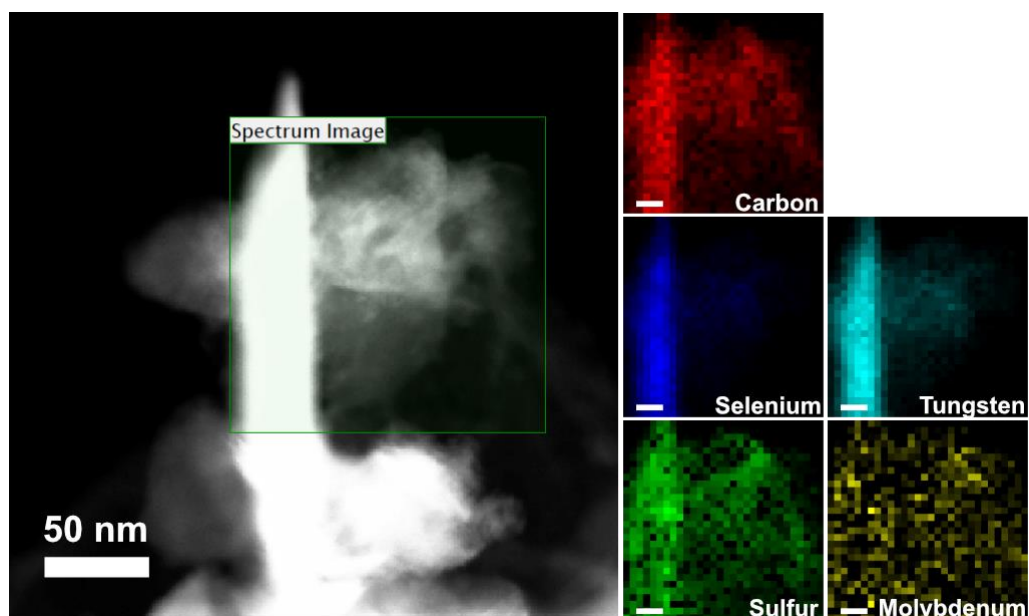**Figure S7: rGO localisation within the co-catalyst-rGO-WSe₂ nanostructured film.**

Figure S7: HAADF and EDS mapping images of Mo_xS_y-rGO-WSe₂ nanostructured film. Free standing rGO spreads out from the WSe₂ nanoflake. The elemental mapping image was carefully taken using high-resolution STEM (ARM-200CF, JEOL Ltd.) equipped with EDS at an accelerating voltage of 80 kV. The scanning rate is 0.1 sec/pix to get the EDS spectrum on each point and the total exposure time is only 6 minutes to reduce electron irradiation damage. Scale bar in EDS mapping image: 20 nm.

Figure S8: Opto-electronic properties of the co-catalyst ultrathin film and of the WSe₂ photoactive materials.
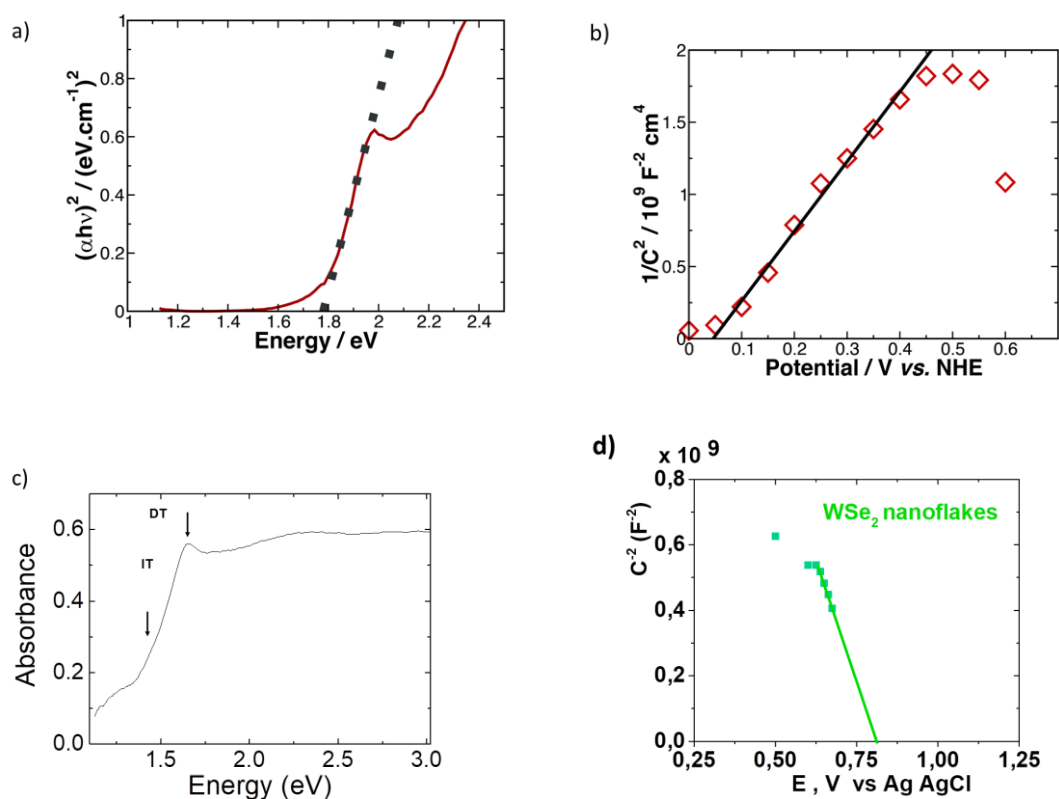

Figure S8. Opto electronic and photo-electrochemical properties of Mo sulfide complex co-catalyst and WSe$_2$ films. a) UV-Vis curve of co-catalyst film deposited on glass substrate. b) Mott-Schottky plot of co-catalyst film on FTO electrode. Electrolyte: Na$_2$SO$_4$ 0.5 M, pH 7. c) Absorbance curve recorded from WSe$_2$ film deposited on glass substrate. Because WSe$_2$ has an indirect gap for nanoflakes displaying thickness larger than a single monolayer, the absorption becomes important only for photons with energies equal or larger than the direct gap transitions denoted DT in the Figure. The transition associated with the indirect gap (denoted IT) which has been extracted from the PL measurement is also reported. Note that the broader peak centered around 2.2 eV is presumably due to transitions associated to the B valence band. d) Mott-Schottky plot recorded on WSe$_2$ film prepared by drop casting on FTO substrate showing a negative slope of the straight line in line with the p-type semi-conduction of WSe$_2$. Electrolyte: H$_2$SO$_4$ 0.5 M. Capacitances were extracted from electrochemical impedance spectra at 1 Hz.

Figure S9: H₂ determination by gas chromatography (GC) and Faradic efficiency determination.

Methods

A closed photo-electrochemical cell equipped with a three electrode set-up was used for the hydrogen detection. An argon flow rate was injected into the cell in order to transport the evolved hydrogen from the photo-electrochemical cell to the Gas Chromatograph (Shimadzu, GC-2014 AT) allowing the real-time analysis of the composition of the gas generated inside the cell. The Faradic efficiency of the photo-electrochemical cell was determined from the calibration curve of the Pt cell. This calibration curve was achieved on the same photo-electrochemical cell, but equipped with Pt foils as both for the working electrode and counter electrode. The Faradic efficiency of our cell is calculated assuming 100 % efficiency for the Pt calibration cell.
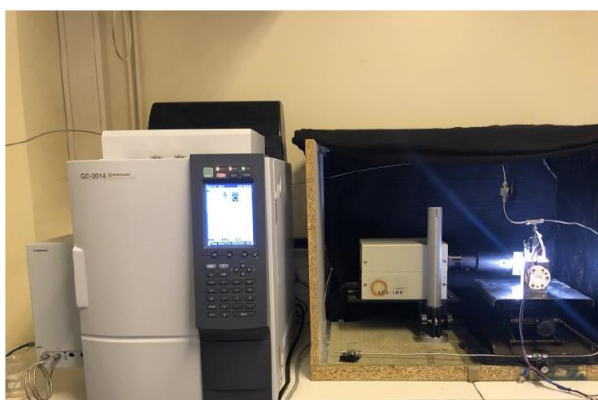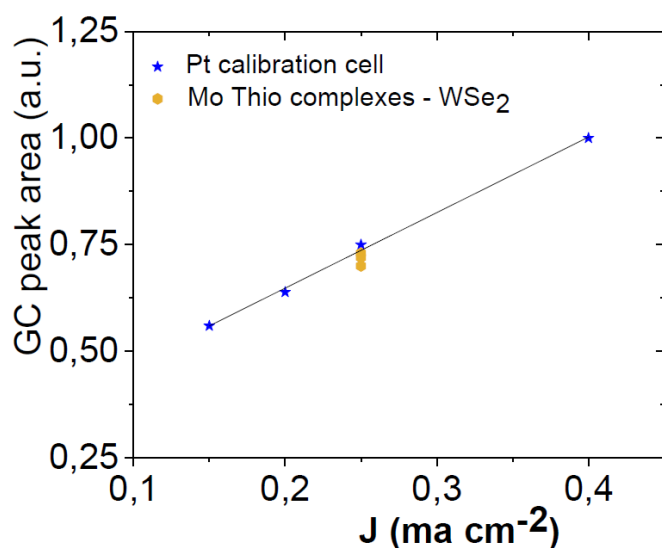

Photograph of H_2 detection

experimental set up.

Figure **S**9: H_2 GC peak areas determined on a Pt electrode (calibration cell) and on WSe_2 photo-electrode activated by thio-, oxo-thio-Mo complexes. Electrolyte: 0.5 M H_2SO_4. Counter electrode: Pt. 1 Sun illumination.

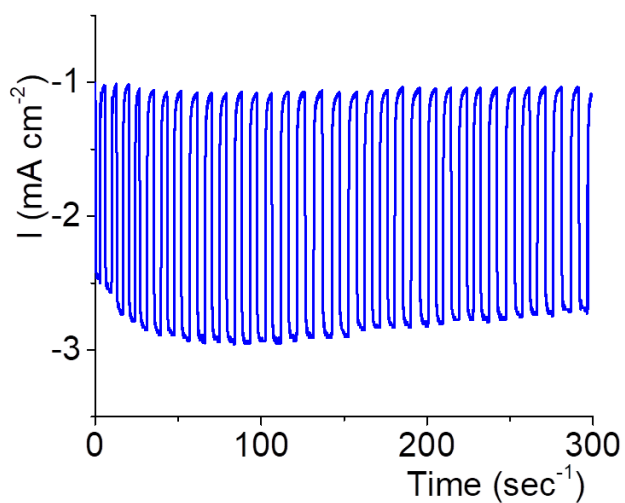*Figure S10: Chrono-amperometry on nanostructured co-catalyst- rGO -WSe$_2$ photo-electrode.*

Figure S10: Chrono-amperometric curve for co catalyst-rGO-WSe$_2$ photo-electrode in H$_2$SO$_4$ 0.5 M. E$_{applied}$= -0.05 V vs NHE. Illumination 1 sun.

Figure S11: Absorbance and incident-photon-to-current (IPCE) spectra of WSe$_2$ based films.
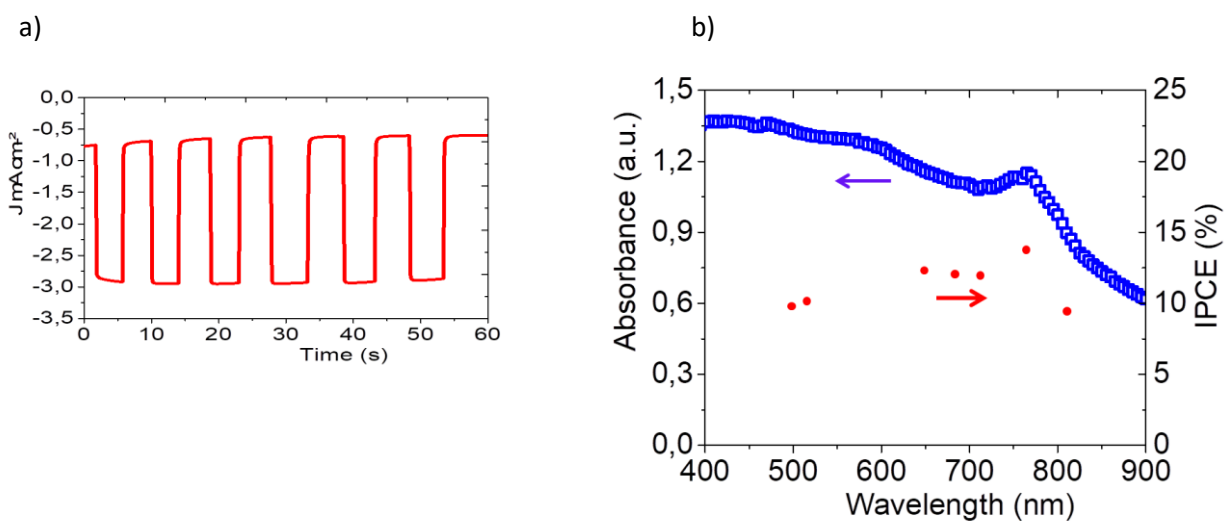
a)

b)

Figure S11: Photon absorption and incident-photon-to-current (IPCE) spectra of WSe_2-based films. a) Typical i(v) curve recorded under intermittent monochromatic illumination (λ = 760 nm) at E= -0.2 V vs NHE b) Absorbance and IPCE spectra of WSe_2-based films. Absorbance was determined from a nanostructured WSe_2 film (e= 1 µm) deposited on a glass substrate.

The absorption curve was determined from transmittance and reflectance spectra recorded on a WSe_2 film (e= 1 µm) prepared from exfoliated nano-flakes by drop casting on a glass substrate. Measurements were performed using a Bentham PVE 300 UV-visible spectrometer, equipped with a dual source Xe/QH (Hydrogen Quartz), TMc 300 triple network monochromator and an integrating sphere for total or diffuse measurements of transmission and reflection.

For IPCE measurements, the distance between the LED and the photocathode was ≈ 30 mm. The spectrum emitted by each LED is centered on a given wavelength with a half width at half maximum of 20 nm with optical power outputs ranging from 20 mW to 400 mW. The naturally diverging beam of the LED has been collimated to a ~ 10 mm diameter beam using special focusing optics designed for coupling the light of high-power LEDs into fiber bundles. The light intensity of each LED has been measured using a calibrated pyranometer Model PMA2144 Digital Class II Pyranometer from SOLAR LIGHT. The intensity sent onto each photocathode has been adjusted for each LED in order to illuminate the photocathode with equivalent intensities for each wavelength, taking into consideration the reflection on the cell facets.

Light absorption and IPCE

The absorbance experimental values, Abs = - Ln (T / 1 – R), were determined from transmittance and reflectance data collected on WSe_2 films drop- cast on a glass substrate. From the absorbance values, we calculated the absorption coefficients α for the various wavelengths from Abs= α e_{eff}. e_{eff} denoting the effective thickness of the film. The effective thickness of our films was estimated from BET pore volume fraction determined on co-textured powder.

Using experimental data of absorbance respectively at λ= 510 and 760 nm (A $_{510\ nm}$= 3.29, A $_{760\ nm}$= 2.81),

λ = 510 nm α $_{\lambda\ 510\ nm}$= 3.29 10^4 cm^{-1}
λ= 760 nm α $_{\lambda\ 760\ nm}$= 2.81 10^4 cm^{-1}

These calculations indicate better light absorption within the nanostructured film for the 500 nm top layer for the shorter wavelength (λ= 510 nm). Unlike to what might be expected, a levelling off of the IPCE values at shorter wavelength is experimentally observed in our film. This may be ascribed to (i) an increased surface recombination of the photo-generated carriers at the top layers or close to the back electrode or to (ii) a non-optimal charge carrier collection to the back electrode due to the large thickness (e= 4 µm) displayed by our nanostructured film.

Figure S12: Electrochemical Impedance spectroscopy (EIS) and Intensity Modulated Photocurrent Spectroscopy (IMPS) of WSe₂-based photo-electrodes.

For EIS measurements under illumination, we used a light emitting diode, Roithner Laser Technik, λ= 450 nm, 1.3 Watt m^{-2}. Irradiance of 1 sun was achieved by adjusting the distance between the sample and the LED and finely controlled using a pyranometer (PMA 2144 Solar light).
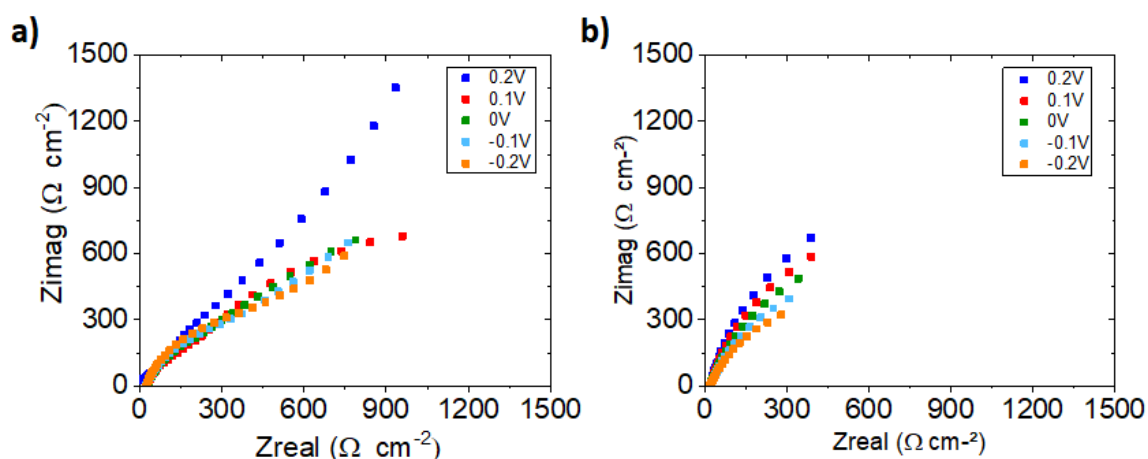

Figure S12-1: Nyquist plots obtained from EIS data of co-catalyst-free WSe₂-based photoelectrodes. a) Drop-cast WSe₂ and b) Nanostructured rGO-WSe₂ photo-electrodes. Electrolyte: 0.5M H₂SO₄. Potential range: from 0.2 to -0.2 V vs NHE; under illumination (λ = 450 nm).
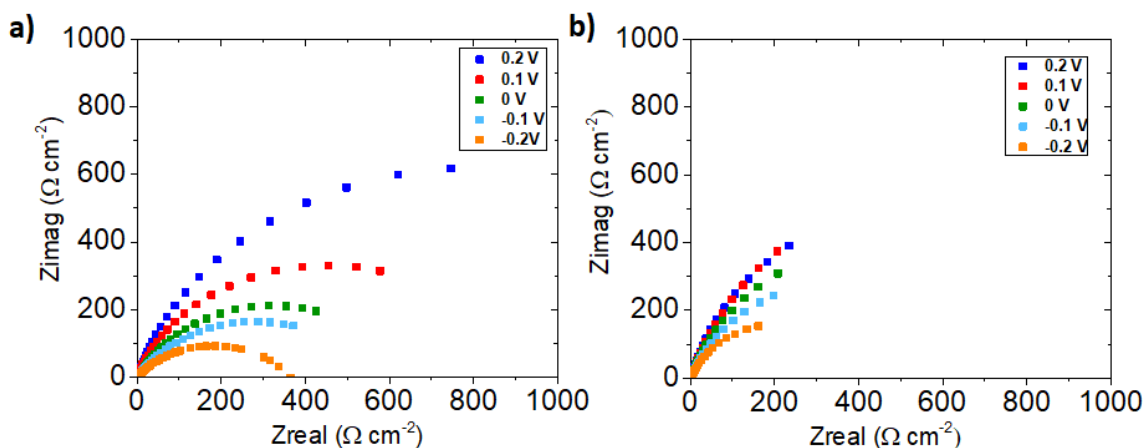

Figure S12-2: Nyquist Plots obtained from EIS data of co-catalyst-coated WSe₂-based photo-electrodes. a) Drop cast Mo$_x$S$_y$ coated -WSe₂ and b) Nanostructured Mo$_x$S$_y$ coated- rGO-WSe₂ photo-electrodes in 0.5 M H₂SO₄. AC impedance measurements were carried out between 0.2 and -0.2 V vs NHE, under illumination (λ = 450 nm).

Charge transfer resistances and capacitances values reported in Figure 4c, d (see main text) were obtained from $R_S - CPE/R_{CT}$ model, where R_S is a series resistance, CPE is a constant phase element and R_{CT} is the charge transfer resistance; the R_S and the CPE are in series while the CPE and the R_{CT} are in parallel (see Figure S12 -3).
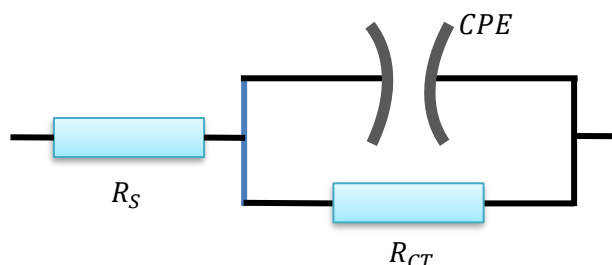

Figure S12-3: Equivalent circuit proposed for the interpretation of the Nyquist plots.

A Simplex method was used to fit the experimental data. The capacitances were calculated from the CPE using the Brug-Formula, as reported below:

$$C = (QR_{CT}^{1-\alpha})^{1/\alpha}$$

Where C is the capacitance (in F); Q (in $\Omega^{-1}.\sec^{\alpha}$) and α are respectively the fitting parameters of the CPE defined as:

$$CPE = \frac{1}{Q(j\omega)^{\alpha}} \text{ in } \Omega$$

The results obtained from the fitting are reported in the following tables, for different applied potentials and for the different photoactive materials, with and without the presence of the MoxSy co-catalyst. R_S, R_{CT}, Q and α are the fitting parameters; C is calculated from R_{CT}, Q and α using Brug Formula (see above). R_{CT} and C values are reported in Figures 4c, 4d (see main text):

rGO/WSe₂

E, V vs NHE	Rs, Ω	R$_{CT}$, Ω	Q, Ω⁻¹.secᵅ	α	C, F
0.2	8.2	2280	0.00176	0.89	0.00208
0.1	5.0	1870	0.00184	0.88	0.00219
0.0	4.2	1552	0.00215	0.86	0.00262
-0.1	4.5	1212	0.00248	0.84	0.00304
-0.2	4.4	964	0.00280	0.83	0.00344

rGO/WSe₂/co-cat MoxSy

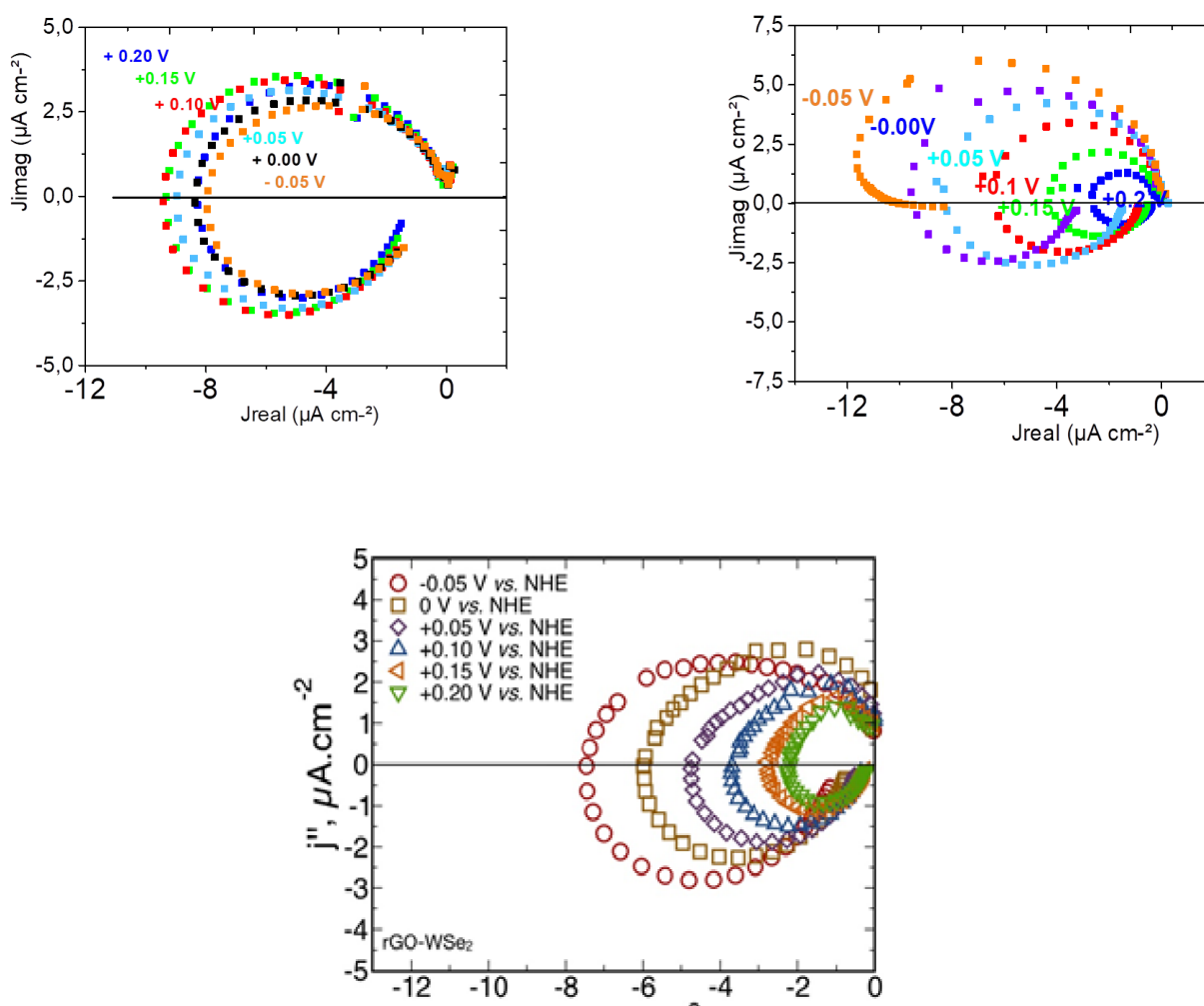| E, V vs NHE	Rs, Ω	R_{CT}, Ω	Q, $\Omega^{-1}.sec^{\alpha}$	α	C, F
0.2	4.34	1513	0.00300	0.85	0.00391
0.1	4.55	1623	0.00274	0.86	0.00350
0.0	4.19	603	0.00441	0.82	0.00543
-0.1	4.37	289	0.00619	0.84	0.00692
-0.2	4.10	29	0.01089	0.88	0.00924

Figure S12-4: IMPS plots of WSe₂-based photo-electrodes. Top left) Drop-cast, catalyst-free/ rGO-free/ WSe₂. Top right) Drop-cast, co-catalyst-coated/ rGO free/ WSe₂ photo-electrodes. Down) nanostructured, catalyst-free, WSe₂/rGO photo-electrode. Electrolyte: H₂SO₄ 0.5 M, Applied voltages are reported vs NHE. Modulated illumination was provided by a light-emitting diode with a wavelength of λ = 680 nm. k_{tr}, k_{rec} values extracted from these plots are reported Figure 4 g, h in the main text.

Figure S13: Slab and edge models of DFT calculations.

In the present work for all the calculations we have used VASP[1-4], an electronic structure code based on the projector-augmented wave (PAW)[5-6] scheme. The PBE [7] exchange-correlation functional was applied, and the influence of van der Waals forces on the optimized geometries was checked by performing PBE-D3[8] calculations. Minor changes in the geometries were observed, and only global constant shift around -0.6 eV in the energy was obtained when comparing PBE-D3 and PBE energies. Since for all substrate configurations strong chemical adsorption were obtained, we have decided to report only PBE results in the present work, to estimate Gibbs free energy of H adsorption, used as a good descriptor of HER activity as proposed in the work of Norskov *et al*[9]

Gibbs free energy estimates were performed using in-house software, using a methodology detailed in Ref. 10.

The cut-off energy is set to 400 eV, with energy criterium of convergence of 10^{-5} for optimization process when a tighter one was used 10^{-8} for frequency calculations. The force convergence criterium was set to 0.01 eV/Å when all the atoms were allowed to relax. A Gaussian smearing of 0.05 eV width is used, with a (2x2x1) Γ-centred grid for Brillouin zone integration for all geometry optimization runs. To build our edges models, our starting point was a 2H-bulk WSe_2 structure made of a (5x5x4) supercell, then cutting the structure and add vacuum to separate the sheets by around 16 Å along z axis.

References

1- G. Kresse, J. Hafner, *Phys. Rev. B*, 1993, **47,** 558(R).
2- G. Kresse, J. Hafner, *Phys. Rev. B*, 1994, **49,** 14251–14269.
3- G. Kresse, J. Furthmüller, *Comput. Mater. Sci.*, 1996, **6,** 15–50.
4- G. Kresse, J. Furthmüller, *Phys. Rev. B*, 1996, **54,** 11169–11186.
5- P. E. Blöchl, *Phys. Rev. B*, 1994, **50,** 17953.
6- G. Kresse, D. Joubert, *Phys. Rev. B, 1999,* **59,** 1758–1775.
7- J. P. Perdew, K. Burke, M. Ernzerhof, *Phys. Rev. Lett* 1996, **77,** 3865; *Phys. Rev. Lett*. 1997, **78**, 1396.
8- S. Grimme, J. Antony, S. Ehrlich, H. Krieg, *J. Chem. Phys.* 2010, **132,** 154104–19.
9- J. K. Nørskov, ,T. Bligaard, A. Logadottir, J. R. Kitchin, J. G. Chen, S. Pandelov, U. Stimming, *J. Electrochem. Soc.* 2005, **152,** 3, J 23–6.
10- J. Barros Barbosa, P. L. Taberna, V. Bourdon, I. C. Gerber, R. Poteau, A. Balocchi, X. Marie, J. Esvan, P. Puech, A. Barnabé, L. Da Gama Fernandes Vieira, I.-T. Moraru, J. Y. Chane-Ching,, Appl. Catal. B Environ**.** 2020, **278**, 119288.
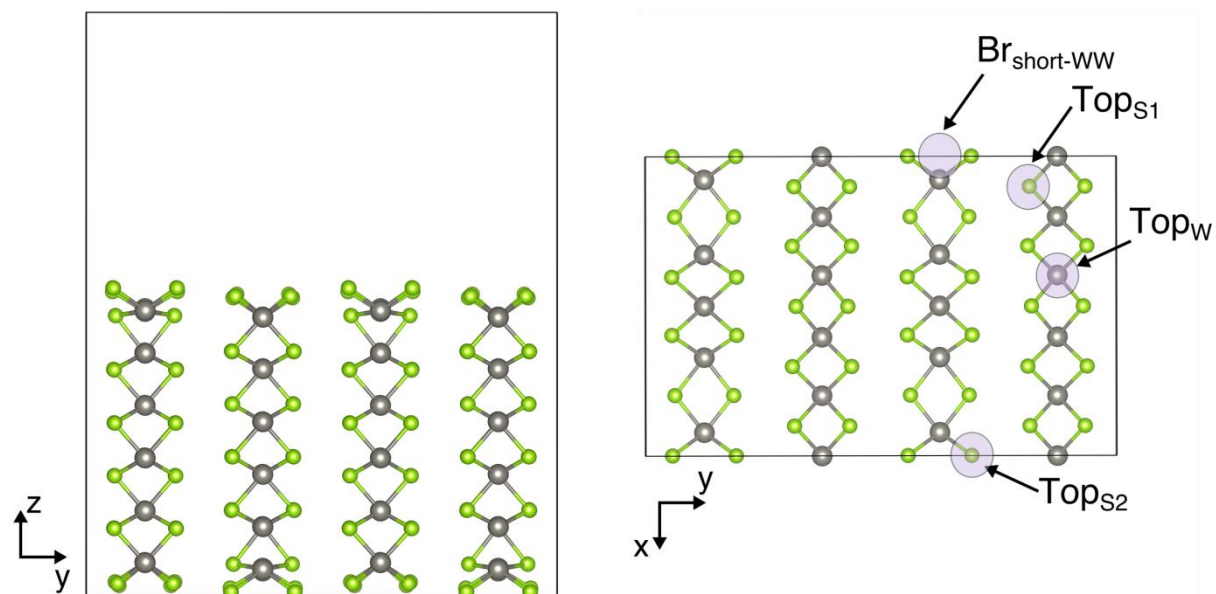
Figure S13. Left panel: side view of the slab model, the black line represents the cell parameter. Se atoms are in green, W in gray. Right Panel: top view of the edge model, with the identification of three distinct adsorption sites.